Geochemical and granulometric fingerprints of 8,200-year Westerly variability recorded in inner-fjord lake sediments from Central Svalbard

Zofia Stachowska [1*], Willem G. M. van der Bilt [2], Jan Kavan [3], Mark F. A. Furze [4], Ingunn H. Thorseth [5] and Mateusz C. Strzelecki [6]

[1*] *zofia.stachowska@usz.edu.pl, Institute of Marine and Environmental Sciences, Doctoral School, University of Szczecin, ul. Mickiewicza 16, 70-383 Szczecin, Poland*

[2] *willemvanderbilt@uib.no, Department of Earth Science and Bjerknes Centre for Climate Research, University of Bergen, Allégaten 41, 5007 Bergen, Norway*

[3] *jan.kavan.cb@gmail.com, Centre for Polar Ecology, Faculty of Science, University of South Bohemia, Na Zlaté stoce 3, 370 05 České Budějovice, Czechia*

[4] *markf@unis.no, Department of Arctic Geology, The University Centre in Svalbard, P.O. Box 156 N-9171, Longyearbyen, Norway*

[5] *ingunn.thorseth@uib.no, Centre for Deep Sea Research, Department of Earth Science, University of Bergen, Allégaten 41, 5007 Bergen, Norway*

[6] *mateusz.strzelecki@uwr.edu.pl, Alfred Jahn Cold Regions Research Centre, Institute of Geography and Regional Development, University of Wrocław, ul. Fryderyka Joliot-Curie 12, 50-383 Wrocław, Poland*

This paper is a non-peer-reviewed preprint submitted to EarthArXiv. This original paper was submitted to *Boreas* for peer review on April 3, 2026.

Abstract

The Arctic is warming faster than any other region on Earth. As sea-ice diminishes, surface boundary conditions (roughness and air-sea coupling) change and open-water fetch increases, potentially strengthening the effective wind forcing on Arctic coasts. These changes can be recorded in lake sediments through the deposition of wind-blown grains and elements, offering insights into past wind and climate dynamics. We reconstruct ca. 8,200 yrs of wind-climate variability using laminated sediments from a closed-basin lake in the Central part of the High Arctic Svalbard archipelago. By integrating geochemical, visual, and granulometric fingerprints within a multiproxy geostatistical framework, we link wind-blown minerogenic input to specific catchment sources and show that iron (Fe)- and titanium (Ti)- enriched clasts originate from distinct dolerite outcrops West of the lake, upwind of the dominant summer Westerlies. These results reveal a locally filtered Westerly input, consistent with valley-fjord channelling. We identify four Mid- and Late Holocene phases of enhanced eolian activity that occurred during intervals when local boundary conditions favoured the entrainment and transport of sediment into the basin. Unit-scale sedimentation shifts can be placed at the end of the Holocene optimum and at the stepwise onset of the Neoglacial. However, the reconstructed wind signal shows comparatively stable long-term behaviour and no direct correspondence with paleoclimate records.

Keywords: Westerly winds, Lake sediments, Spitsbergen, Holocene, Sediment provenance, End Member Modelling

1. Introduction

The Arctic is warming at nearly four times the global average – a phenomenon known as Arctic amplification (Rantanen et al., 2022). This rapid warming leads to cryosphere degradation, which enhances the supply of unconsolidated material available for eolian transport. Yet the geomorphic response to a warmer Arctic is unlikely to be monotonic, because sea-ice not only limits fetch and coastal exposure, but also mediates momentum transfer and effective surface forcing (Muilwijk et al., 2024). While wind is a primary driver of Arctic geomorphic change, instrumental observations provide only a brief baseline for High Arctic wind variability (Rasmussen et al., 2023; Rymer et al., 2022; St. Louis et al., 2024). Paleoenvironmental archives are therefore essential for extending these time series and testing how eolian erosion thresholds and depositional filtering of eolian input vary across different climate states (Kylander et al., 2023; Stachowska et al., 2024). Lacustrine sediments are particularly valuable, as they trap wind-blown mineral particles preserved as changes in minerogenic flux, density, and grain size (Hess et al., 2023; Saunders et al., 2018; Stachowska et al., 2024). In settings with contrasting catchment sources, this signal can be isolated by combining high-resolution core scanning with granulometric unmixing and source validation (Stachowska et al., 2024). Here, we apply that workflow to identify provenance-specific eolian input in a topographically complex Arctic setting.

We investigate Dunsappietjørna, a lake in Gipsdalen, a valley in Central Spitsbergen (Svalbard). This study area lies within the climatic boundary between the North Atlantic and the Arctic Ocean (Farnsworth et al., 2020), and the archipelago is recognised as an Arctic climate-change hotspot, having warmed by ~4°C over the past century (Førland et al., 2011; Nordli et al., 2020). Postglacial isostatic uplift here generally exceeds global sea-level rise,

resulting in continuous Holocene sedimentary archives (Salvigsen, 1984; Stachowska et al., 2024; Strzelecki et al., 2026). We target a lake in this inner fjord-valley system to test how local topography, sea-ice-modulated exposure, and sediment availability shape the translation of atmospheric variability into a depositional signal. Modern observations from Isfjorden show pronounced spatial heterogeneity in near-surface wind direction and speed, driven by valley-fjord geometry, land-sea contrasts, and air-sea-ice interactions, making this setting suitable for evaluating local filtering of a broader wind signal (Frank et al., 2023a, 2025). Our study area also contains seasonally reworked sediments derived from contrasting sedimentary and igneous lithologies (Dallmann, 2015; NPI Geological maps, 2026), offering a foundation for examining how atmospheric regimes manifest in sheltered, topographically complex locations.

This study presents a ca. 8,200-year-long archive of summer Westerly winds reconstructed from Dunsappietjørna sediments (Fig. 1B). By applying a multiproxy approach, we link downcore changes in eolian clastic input to Fe-Ti-rich grains derived from local dolerite outcrops West of the lake (Dallmann, 2015; NPI Geological maps, 2026; Senger et al., 2014), providing a diagnostic provenance target for wind-blown minerogenic input. We distinguish the eolian component from other parallel depositional processes and test whether the record expresses broader atmospheric forcings or a locally filtered signal imposed by inner-fjord-valley geometry, sea-ice-modulated exposure (Frank et al., 2025), and changes in sediment availability (Strzelecki et al., 2026). We then compare major transitions in the Dunsappietjørna record with selected local and regional records of Holocene glacial activity (Farnsworth et al., 2020; Forwick et al., 2010), sea-ice, ice rafting, and temperature (Kong et al., 2025; Müller et al., 2012a, b; Rasmussen et al., 2012), and try to evaluate how these boundary conditions influence sediment entrainment and depositional filtering in inner-fjord settings – an issue of increasing importance as Arctic warming alters wind patterns and coastal exposure.

2. Study area

Gipsdalen, situated in Bünsow Land, on Central Spitsbergen, is ~25 km long and ~3 km wide U-shaped valley (Fig. 1C). Several outlet glaciers head into the valley (e.g., Florabreen, Margaretbreen, Methuenbreen, Boltonbreen, and Stenhousebreen), all located on the surrounding plateau and in proximity to the Filchnerfonna (East) and Lomonosovfonna (North) ice caps (Fig. 1C; Brekke and Hansson, 1990; Dallmann, 2015; Forwick et al., 2010). The bedrock comprises Late Carboniferous to Early Permian sedimentary rocks from the Billefjorden, Gipsdalen, and Tempelfjorden Groups (limestone, dolomite, gypsum, marl, sandstone and coal-bearing shale; Brekke and Hansson, 1990; Dallmann, 2015). In contrast, the Early Cretaceous dolerites of the Diabasodden Suite (Nejbert et al., 2011; NPI Geological maps, 2026; Senger et al., 2014), typically medium- to fine-grained and containing Fe and Ti oxides, such as ilmenite and titanomagnetite (Nejbert et al., 2011; Senger et al., 2014), outcrop at several localities in Eastern and Southeastern Isfjorden. Out of these, the largest, located closest to the catchment, lie at Gisphukodden, a coastal promontory Northwest of the valley, as well as on Gåsøyane, and at Kapp Thordsen, Northwest of Gipsvika (Fig. 1C), West of the catchment (Brekke and Hansson, 1990; Nejbert et al., 2011; NPI Geological maps, 2026; Senger et al., 2014).

Our study site, Dunsappietjørna (78º27'N, 16º41'E, ~65 m a.s.l.), is a small, shallow basin (0.06 km^2, ~3.3 m deep) located in Southeastern Gipsdalen, within a sparsely vegetated raised shoreline complex on the coast of Gipsvika (Fig. 1C-E). Local relative sea-level (RSL) records from inner Isfjorden document rapid Early Holocene postglacial emergence and continued RSL fall. While the available curves do not permit a precise isolation age for a basin at ~65 m a.s.l.,

121 they do indicate that it occurred in the Early Holocene (Forman et al., 2004; Salvigsen, 1984;
122 Strzelecki et al., 2026). An independent emergence constraint from Petuniabukta (Billefjorden),
123 where a whale bone was found at 58.1 m a.s.l., and dated back to 10,300 cal. yrs B.P., suggests
124 that 65 m a.s.l. could correspond to ca. 10,700 cal. yrs B.P. (Lulák et al., 2026). Geomorphic
125 constraints for inner Isfjorden indicate a postglacial marine limit of at least ~72 m a.s.l. (Forman
126 et al., 2004; Salvigsen, 1984; Strzelecki et al., 2026). Following emergence, the lake's basin
127 likely formed within a shallow fjord embayment. As shown in Figs. 1D-E and S1A, it is
128 dammed by sandy-to-gravelly beach-ridges with inter-ridge marsh complexes containing
129 occasional silty layers. Clayey-silty marine deposits occur landward of the ridges, and
130 gelifluction material covers the valley sides. The Gipsdalselva system includes active alluvial
131 reaches and floodplains, including Leirflata – a floodplain located Northwest of the lake. A
132 sandy-gravelly alluvial fan borders the beach-ridge system to the Southwest. Numerous sand-
133 dominated eolian deposits are also present in this part of the valley, particularly North of the
134 Gipsdalselva mouth, around Leirflata, and farther into Gipsdalen (Figs. 1D-E and S1A; Brekke
135 and Hansson, 1990).
136
137 Data from 1991-2020 C.E. show that the mean annual air temperature at the Svalbard Lufthavn
138 weather station (~33 km Southwest) remained below freezing (around -4°C), with an average
139 annual precipitation of ~200 mm (MET Norway, 2026), which is consistent with the broader
140 climatic characterisation of Central Svalbard (Førland et al., 2011). The long-term observational
141 record (1981-2010) by Førland et al. (2011) further indicates an overall rise in al temperature
142 during recent decades. Sentinel-2 satellite imagery confirms that the lake and the area are
143 typically ice-free from July to September (Fig. S2; ESA, EC, 2023). During fieldwork in March
144 2024, the lake ice surface was not exposed, and the snow cover showed no obvious
145 accumulation of wind-blown sediment. No evidence of water-level drawdown or shoreline

displacement was noted during the field campaigns. However, our field observations and remotely sensed data suggest that the Eastern side of the catchment may be affected by summer meltwater discharge from Dalkallen and Aitkenfjellet, as evidenced by ephemeral streams (Figs. 1D-E, and S1A-B). Wind observations from the Gåsøyane lighthouse station show that the area is influenced by both Westerlies and Easterlies, revealing distinct seasonal patterns (Fig. 1B and 'Supplementary Note 1'). During winter (December-February; DJF), Northerly and Northeasterly winds dominate, with weaker Easterly contributions, while Westerlies are less frequent but have the highest mean speed, averaging 12.3 m/s (a strong breeze). In contrast, summer (June-August; JJA) winds mainly come from the Southwest and Northwest directions and average 5.3 m/s (a gentle breeze), while the Northerly and Northeasterly flow is less frequent but stronger, averaging 7.0 m/s (a moderate breeze; Fig. 1B and 'Supplementary Note 1'). However, Frank et al. (2023b) report that local topographic effects near the weather station amplify measurements for these winds.

3. Material and methods

3.1. Fieldwork

A bathymetric survey of the lake was conducted during the field campaign in September 2023 using a Lowrance Elite-9 Ti^2 fish finder echosounder. We targeted a coring site in a flat central section of Dunsappietjørna's Northwest part, at a water depth of ~3.3 m (see Fig. 1D). Next, we retrieved a ~121 cm-long sediment core DST-2023 GC, using a UWITEC gravity coring system fitted with 9 cm diameter liners. Additionally, during a separate field campaign in July 2024, four catchment samples (CSs) were collected to aid source-to-sink analysis (Figs. 1E and S1): one from an Easterly inlet to the lake (CS 1), two from a fluvial floodplain Northwest of the lake (CS 2 and 4), and one from an alluvial fan Southwest of the lake (CS 3).

171

172 **3.2. Stratigraphy and geochemistry**

173

174 Following fieldwork, the core was split lengthwise at the EARTHLAB facility at the University
175 of Bergen (UiB) and stored at 4°C in between analyses. The core was then visually logged and
176 photographed using an optical (RGB) line camera. Next, we performed non-destructive
177 scanning analyses. To map minerogenic element input to Dunsappietjørna, we used an ITRAX
178 X-Ray Fluorescence (XRF) scanner at the EARTHLAB (UiB), equipped with a Chromium (Cr)
179 tube (Cox Analytical System, 2008), set to 40 kV and 10 mA, to detect lighter lithogenic
180 elements that characterise the carbonate-bearing catchment bedrock (Rothwell and Croudace,
181 2015). A total of 25 elements were analysed downcore at 200-µm intervals. Computed
182 Tomography (CT) scanning was subsequently performed to capture downcore variations in
183 density and visualise sediment structure in 3-D, using CT grayscale values (van der Bilt et al.,
184 2018b). Scanning was performed using a ProCon X-ray CT-ALPHA scanner at the
185 EARTHLAB facility (UiB), operated at 120 kV and 800 µA with a 267 ms exposure time, and
186 acquiring 2,400 images per rotation. To minimise the impact of beam hardening (Brooks and
187 Di Chiro, 1976), we applied a 1-mm copper (Cu) filter. Downcore CT grayscale variations were
188 mapped at 500 µm resolution using the SplineProbe tool in Thermo Fisher Avizo version 9.
189 Following non-destructive scanning, we extracted 121 samples for physical analyses at
190 contiguous 1 cm intervals using a 0.3 cm-wide syringe. Samples were dried for 12 hours at
191 105°C to determine Dry Bulk Density (DBD; g/cm^3), and combusted for four hours at 550°C
192 in a muffle furnace to determine organic content by means of Loss on Ignition (LOI, %; Dean,
193 1974; Heiri et al., 2001). Finally, the remaining sample residues, along with four catchment
194 samples (CSs), were analysed for grain-size distribution. For this purpose, we relied on a

Malvern Mastersizer 3000 equipped with a Hydro SV dispersion unit. To ensure reproducibility, each sample was analysed five times (Malvern Panalytical, 2015).

3.3. Chronology

Age control for the core DST-2023 GC was established using radiocarbon (^{14}C) dating, with samples taken near distinct (unit) transitions, as identified by visual logging and core imagery (see the previous section). The extracted material was then wet-sieved using 250 µm and 125 µm meshes, examined, and picked under a Leica MZ6 light microscope at magnifications of 6.3-40x, then dried overnight at 50°C. To reduce freshwater reservoir effects (Philippsen, 2013), we prioritised terrestrial plant macrofossils. Their selection was based solely on preserved morphological features (vascular plant fragments, such as leaves and stems, and seeds). However, because we could collect only three samples of terrestrial plant material, we also collected four samples of aquatic moss. We paired them with terrestrial material in two same-depth intervals and one adjacent interval because the dry weights of the terrestrial fragments were low (Table 1), and to also screen for potential hardwater effects. The material was submitted for Accelerator Mass Spectrometer (AMS) dating, with six samples sent to the Poznań Radiocarbon Laboratory in Poland (Poz) in December 2023 (Goslar et al., 2004), and one to the Tandem Laboratory at Uppsala University in Sweden (Ua; Table 1) in October 2024.

We established chronological control for the ~120.5 cm-long DST-2023-GC record by generating an age-depth model, based on seven AMS ^{14}C dates (Fig. 2B; Table 1). We used the Bayesian Bacon R package v.3.3.1 (Blaauw et al., 2022), calibrated ^{14}C ages using the IntCal20 Northern Hemisphere calibration curve (Reimer et al., 2020), and reported a 2σ (95%)

confidence range (cal. yrs B.P.; Fig. 2A, Table 1). The core top was assigned a zero age (2023 C.E. – the year of core extraction).

3.4. Statistics

Since the core compressed by ~5 cm during CT scanning in an upright position, we linearly tuned the CT grayscale to previously measured DBD values, as both parameters reflect sediment density (Fig. 3B; van der Bilt et al., 2018b), and the latter retained the original depth scale. We standardised the data to z-scores before defining tie-points at major corresponding trends and applied linear interpolation between tie-points using QAnalySeries software (Kotov and Pälike, 2018). Next, we resampled the corrected CT grayscale values at a 500 μm in PAST v. 4 (Hammer et al., 2001), consistent with the input resolution.

We only considered XRF elements with medium to high sensitivity to the fitted Cr tube and a Signal-to-Noise ratio (SNR; μ/σ) ≥1 (Montgomery, 2017). We applied a centred-log ratio (clr) transformation to remove closed-sum effects and minimise matrix-related artefacts (e.g., variability in water content, grain-size, porosity, and organic matter), allowing statistical comparison of inter-element relationships and robust identification of sediment sources (Bertrand et al., 2024). The transformation was performed in the CoDaPack software (Thió-Henestrosa and Comas, 2011).

Grain-size statistics, expressed as metric (μm) Folk and Ward values, were calculated using the GRADISTAT software (Blott and Pye, 2001). We then applied End Member Modelling Analysis (EMMA) to unmix particle size distributions and disentangle eolian sediment sources

(Paterson and Heslop, 2015; Prins and Weltje, 1999), using AnalySize v. 1.2.2 in MATLAB (Paterson and Heslop, 2015). We employed the non-parametric HALS-NMF algorithm because it is well-suited for grain-size unmixing and disentangling depositional processes, and reproduces the physically meaningful and plausible End Members (EMs; Paterson and Heslop, 2015). To ground-truth our EMs, we measured grain-size in catchment samples (CS 1-4) and tested whether their distributions matched the EM modes.

To enable statistical analyses on a shared 0.5 cm resolution with physical measurements, XRF and CT grayscale data were smoothed (using 25- and 10-point moving averages, respectively), then resampled in PAST v. 4 (Hammer et al., 2001). Using the same software, we first calculated Spearman's rank correlation coefficients (ρ), then applied cross-correlations (r) to address potential offsets between physical measurements and scanning data. Previously, EMMA-derived EMs were transformed to the logarithm (log), following the recommendations of Bertrand et al. (2024). We then examined the shared gradients of change among selected proxy parameters in the DST-2023 GC using Principal Component Analysis (PCA). The analysis was performed on the following variables: CT grayscale, DBD, LOI, clr Fe, Ti, and Ca, and log EM 1-3 abundances, with the input data standardised beforehand, following the PAST v. 4 manual (Hammer et al., 2001).

3.5. Scanning Electron Microscopy and Energy Dispersive X-ray Spectroscopy

We used Scanning Electron Microscopy (SEM) to obtain high-resolution images of the sediment matrix, authigenic phases and individual clastic grains, including their surface features (Itamiya et al., 2019; Marshall et al., 2012; Vos et al., 2014). We also used Energy-Dispersive

X-ray Spectroscopy (SEM-EDS) to map and quantify elemental and oxide compositions at the grain level (Newbury and Ritchie, 2015).

Overall, we examined 12 downcore samples and two catchment samples (CSs) representing the Eastern inlet (CS 1), and the Western alluvial plain (CS 2; see also 'Study area' and Figs. 1D; S1A-C). Initially, to identify the main lithological variability and obtain SEM imagery, we collected five bulk sediment samples (10.5, 36.5, 80.5, 104.5, and 113.5 cm; 1 ml each) from each key lithological unit (see our 'Stratigraphy and geochemistry' section). Next, to test the EMMA- and XRF-based provenance interpretation at the grain-size scale, we also targeted six samples containing leftover material from grain-size measurements (8.5, 79.5, 81.5, 82.5, 116.5, and 117.5 cm) and one from the vegetation mat at a depth of 1.5 cm, along with CSs 1-2. These samples were separated into two size fractions prior to analysis, to characterise grain-size compositional and morphological properties relevant to potential provenance: the <20 µm material was used to assess the elemental composition and morphology of clastic carbonates, while the >20 µm material was targeted to map oxide compositions and morphology of Fe-Ti-rich clasts. In both cases, SEM-EDS spectra were collected from individual grains.

All samples were prepared at the EARTHLAB facility at UiB and analysed at the ELMILAB, UiB. Before analysis, we dried bulk sediment samples for 12 hours at 50°C. Leftover material from grain-size analysis was additionally sonicated in distilled water for 60 s, filtered through 20 µm polycarbonate membranes mounted in 5 ml Eppendorf tubes, and then dried under the same conditions as bulk sediment samples. All samples were mounted on aluminium stubs with adhesive carbon (C) tape and coated using an Agar Turbo Carbon Coater.

We used a ZEISS SUPRA 55VP SEM equipped with a Thermo Scientific Noran System 7 EDS with Pathfinder X-ray Microanalysis software v. 2.11. SEM-EDS and SEM imagery of the <20 µm fraction were conducted under high-vacuum conditions at 15 kV, a working distance of ~8.5 mm, and a dwell lifetime of 30 s for EDS analyses. For the imagery, we selected a secondary electron (SE2) detector, and magnifications ranging from ~3,000 to ~21,000. To improve surface resolution and reduce charging artefacts, the >20 µm fraction and bulk samples were imaged at an accelerating voltage of 5 kV and with a working distance of ~5.8-6.0 mm. We also excluded C and oxygen (O) via manual deselection in Pathfinder v. 2.11 for all EDS analyses, and converted the results to oxides (wt%).

To compare our oxides with the dolerite oxide record from Kapp Thordsen (CS-23) and Gåsøyane (CS-24; Nejbert et al., 2011), we only targeted clasts in the >20 µm fraction that fell within the $\pm 2\sigma$ grain-size window of EM 3 (the coarse-silt EM interpreted as eolian component in this study – see section 4.3) to restrict the SEM-EDS comparison to grains most representative of that EM, and therefore avoid biasing by different fractions. This retained 24% of the initially mapped clasts and limited the focus to 59 spectra (typically 5-6 per clast). We then normalised both wt% datasets to a common subset: Na_2O, MgO, Al_2O_3, SiO_2, P_2O_5, K_2O, CaO, TiO_2, MnO, and Fe_2O_3. Because the reference dataset reports total Fe only as Fe_2O_3 (Nejbert et al., 2011) while we obtained only FeO, we calculated Fe_2O_3 values by multiplying FeO concentrations by a stoichiometric factor of 1.111 (Element — Oxide Conversions, 2023).

3.6. Mapping

All spatial analyses were performed in QGIS 3.34 (Nyall Dawson et al., 2026), including bathymetry post-processing and generating isobaths. We used ArcticDEM at 2 m resolution (Porter et al., 2023) after correcting the offset between ellipsoid and geoid heights for altitude-related calculations. The same tool was used to quantify the hypsometry of mapped dolerite outcrops (Fig. 1C), with the areal extent of 5 m altitude bins calculated separately for Gåsøyane and Gipshuksletta (3.5 km^2), and for the combined area including Kapp Thordsen (13.4 km^2). A high-resolution orthophotography of Dunsappietjørna and its surroundings was processed using a DJI Mavic 3E drone equipped with a Real Time Kinematic Global Navigation Satellite System (RTK GNSS) module, following the workflow presented by Strzelecki et al. (2026). The locations of the main geological units were obtained from the Norwegian Polar Institute server (NPI Svalbardkartet, 2026), as were the background orthoimage and vector topography shapefiles.

4. Results and discussion

4.1. Core chronology

Constrained by four accelerator mass spectrometry (AMS) ^{14}C dates, the Bayesian age-depth model reveals that the recovered sequence spans the last ca. 8,200 cal. yrs B.P. (the Mid- and Late Holocene). Three anomalously young ages relative to their stratigraphic positions are identified as outliers (Fig. 2A, Table 1). We exclude the risk of offsets associated with the freshwater reservoir effect (Philippsen, 2013). Instead, as field observations and drone imagery document soft vegetation mats across much of the lake bottom, including the coring site (Fig. 1E), we infer contamination by modern aquatic plant material (observed as dense soft mats

during the fieldwork in March 2024). During gravity coring, these mats were likely folded against the liner walls and dragged upward as the barrel penetrated the sediments.

Based on core logging and Computed Tomography (CT) orthoslices, we did not observe marine macrofossils, erosive contacts or rip-up clast or other macroscopic signs of marine influence in the recovered sequence (Goslin and Clemmensen, 2017), consistent with the local sea-level history and suggesting the timing of lake isolation to at least ca. 10,700 cal. yrs B.P. (see our 'Study area'; Forman et al., 2004; Lulák et al., 2026; Salvigsen, 1984; Strzelecki et al., 2026). With our modelled basal age at ca. 8,200 cal. yrs B.P., this indicates that at least 2,500 yrs of the earliest postglacial sediments were not retrieved (Fig. 2C).

SAR peaks at ~0.27 mm/yr between ca. 8,200-7,000 cal. yrs B.P. (Fig. 2B), overlapping with the early phase of the Mid- Holocene deceleration in relative sea-level (RSL) fall reconstructed from the adjacent Bjonasletta beach-ridge plain (Fig. 1B), which documents three major phases of Holocene RSL regression (Fig. 2C; Strzelecki et al., 2026). Our observations are consistent with higher sediment supply during catchment adjustment following deglaciation. Around ca. 7,000 cal. yrs B.P., SAR drops sharply and remains lower thereafter, consistent with reduced changes in basin-shoreline geometry and slower RSL fall (Forman et al., 2004; Salvigsen, 1984; Strzelecki et al., 2026).

4.2. The Mid- and Late Holocene evolution of Dunsappietjørna

4.2.1. Core stratigraphy

The Dunsappietjørna core comprises dark-brown, homogeneous, fine-grained sediments with light-beige, fine-grained laminae that range in thickness from ~1.5-2 mm to ~1-2 cm. We

designate three main lithological units (1-3; Fig. 3), and use a change in laminae thickness and resolution, shown in CT orthoslices and RGB imagery, to define the boundary between units 3 and 2, which coincides with a shift in lithogenic elemental values, expressed by centred-log ratios (clr) of titanium (Ti), iron (Fe), and calcium (Ca). We also observe a more subtle shift in lamina thickness and resolution concurrent with changes in lithogenic elemental values between units 2 and 1, accompanied by a marked change in organic content (Loss On Ignition, LOI, %; Dean, 1974; Heiri et al., 2001). We further subdivide units 3 and 1 into subunits a-b (Fig. 3), based on finer-scale variations in lamination and lamina thickness, shifts in the relationship between clr Ti-Fe and clr Ca, as well as changes in organic content and sediment density. Principal Component Analysis (PCA) supports this unit classification, with samples clustering within the unit boundaries in the PCA ordination space (Fig. 4). Units are then contextualised by the regional and local records of Mid- and Late Holocene climate variability. We also note two distinct dark intervals at the depths of ~91.5-96.5 cm, and ~0-2.5 cm, both characterised by high LOI and low density (Fig. 3B). Corresponding to vegetation mats on the lake bottom (see the 'Core chronology'), they are excluded from further interpretations.

While Mean Grain-Size (MGS, μm) is dominated by medium-silt throughout the whole core, End Member Modelling Analysis (EMMA) reveals three End Members (EMs; Dietze et al., 2022; Paterson and Heslop, 2015; Prins and Weltje, 1999): medium-silt-sized EMs 1-2 (μ=9, and 16 μm, respectively), and coarse-silt EM 3 (μ=27 μm; Figs. 3B-C and S4B). Clr Ti – a robust proxy for terrigenous material – is closely tracked by clr Fe (Fig. 3B; Auer et al., 2025; Stachowska et al., 2024). This is consistent with a shared minerogenic control and supported by their strong positive correlation (ρ=0.89; p≤0.05; n=2,278; Table 2 and Fig. S3). Both are also moderately correlated with MGS (ρ=0.49, 0.44, respectively; p≤0.05; n=112), and CT grayscale (ρ=0.54, 0.30; p≤0.05; n=2,260), and they also exhibit statistically significant but

weak to moderate correlation with EM 3 (ρ=0.33, 0.40, respectively; $p \leq 0.05$; n=109). Additionally, EM 3 grain-size distribution resembles that of catchment sample (CS) 2, sourced from the alluvial plain West of the lake (see Figs. 1E and 3C, as well as the 'Study area', and 'Methods'). SEM imagery and SEM-EDS reveal Ti- and Fe-rich minerogenic phases >20 μm in size, selected to minimise influence from neighbouring EM 2 and coarser clasts. With sizes of ~23-31 μm, all grains fall within the $\pm 2\sigma$ grain-size window of EM 3, and likely include rutile (TiO_2), augite (clinopyroxene), and chlorite (hydrous phyllosilicate; Fig. 5E-H and Table S3). However, because Fe is redox-sensitive (Bertrand et al., 2024; Davies et al., 2015; Kylander et al., 2011), we cannot rule out a non-detrital component of its variability, reflected in the log(Fe/Ti) ratio (Fig. S5; Bertrand et al., 2024). Meanwhile, clr Ca reflects mixed carbonate deposition, as SEM imagery and SEM-EDS identify both authigenic (Fig. 5A-B) and clastic carbonates (Fig. 5C-D; Table S3). We associate the authigenic component with seasonal in-lake precipitation that occurs during hardwater whiting conditions – a phenomenon most pronounced in summer, when rising water temperatures reduce calcite solubility, promoting precipitation (see also 'Supplementary Note 2'; Küchler-Krischun and Kleiner, 1990; Mazurek et al., 2012; Ohlendorf and Sturm, 2001). Located on carbonate-rich bedrock, Tundra Lakes in Petuniabukta (~30 km Northwest of Dunsappietjørna) exhibit peak summer water temperatures exceeding 10°C (July-August), and pH conditions that favour calcite precipitation. As Tundra Lakes provide a local analogue for conditions that can favour seasonal carbonate precipitation in cold, hardwater lakes (Mazurek et al., 2012), we infer a similar mechanism in Dunsappietjørna. We also observe that clr Ca is not linked to minerogenic control in the same way as clr Ti-Fe, as indicated by their anticorrelation (ρ=-0.94 and -0.95, respectively; $p \leq 0.05$; n=2,278). It also anticorrelates with EM 3 (ρ=-0.42, $p \leq 0.05$, n=109) but shows a weak positive correlation with both EM 1 (ρ=0.21, $p \leq 0.05$, n=111) and 2 (ρ=0.22, $p \leq 0.05$, n=110). Given the predominance of carbonate rocks in the local bedrock (Brekke and Hansson, 1990; Dallmann,

412 2015), we test the presence of clastic carbonates in our core record. SEM imagery and SEM-
413 EDS reveal clastic dolomite and calcite crystals <20 μm in size (Fig. 5C-D and Table S3),
414 corresponding to most of the ±2σ grain-size range of EM 2. We also note that EM 2 grain-size
415 distribution bears resemblance to that of CS 1 (Figs. 3C and S6), collected from the clayey-
416 silty, carbonate-rich Eastern inlet to the lake that is active during the melt season (see also
417 'Study area', and Figs. 1D-E and S1A-B). Meanwhile, we tie EM 1 abundance to SEM-
418 identified authigenic carbonate phases. Without microfacies characterisation or an independent
419 annual chronology and seasonal markers, we do not interpret laminations in our lake record as
420 varves, even though varved lake sediments form when depositional processes are strongly
421 seasonal, and laminae are preserved under sustained absence of sediment mixing, e.g., under
422 limited wave reworking and bioturbation (Zolitschka et al., 2015). Consistent with best
423 practices outlined by Zolitschka et al. (2015), an annual signal cannot be established from visual
424 lamination alone and requires independent verification with complementary evidence.
425 Accordingly, we interpret the co-occurrence of carbonate phases and light laminae in our lake
426 archive as most likely consistent with short-duration hardwater precipitation pulses during the
427 ice-free season. In contrast, the more minerogenic, higher-density background could also
428 accommodate detrital runoff carbonate input. However, the current dataset does not
429 discriminate whether individual laminae reflect recurring seasonal processes or event
430 deposition, and we therefore treat lamination frequency as an indicator of depositional
431 variability rather than a sign of annual lamination. Finally, the first two principal components
432 (PCs) summarize 71.47% of the total variance, with PC 1 and PC 2 explaining 37.94% and
433 33.53%, respectively. PC 1 is primarily defined by clr Ti, Fe, and Ca, whereas PC 2 is defined
434 by LOI, log EM 2, DBD and CT grayscale (Fig. 4; Table S1).
435

436 **4.2.2. Climate controls on sedimentation**

Basal unit 3, divided into subunits 3b and 3a, covers 121.44-96.5 cm (Fig. 3). Spanning ca. 8,200-7,300 cal. yrs B.P., the unit covers the transition from the Early to the Mid- Holocene. This is coeval with the highest SAR in Dunsappietjørna archive, which declines in step with local RSL fall (Fig. 2B-C; Strzelecki et al., 2026). Light-beige sediments show high LOI and clr Ca values but limited clastic and dense input. Along with the finest MGS and the highest EM 1 abundance, this is consistent with enhanced authigenic carbonate and organic sedimentation (Figs. 3B-C and S4B), supported by SEM imagery and SEM-EDS evidence for flake-like, anhedral carbonates (Fig. 5B and Table S3). This proxy combination suggests that unit 3 records a late phase of the Holocene Thermal Maximum (HTM), overlapping with the regional glacier minimum ca. 8,000-6,000 cal. yrs. B.P. (Farnsworth et al., 2020), and warmer-than-present conditions in alkenone-inferred lake records from Northern Svalbard shown in Fig. 7F (van der Bilt et al., 2019; Kong et al., 2025), while also being partly in-phase with the first major Mid- Holocene cooling step between ca. 7,800-7,000 cal. yrs B.P. (van der Bilt et al., 2018a). Regional hydroclimate reconstructions from Northern Svalbard further indicate winter-dominated precipitation until ca. 6,000 cal. yrs B.P, under enhanced moisture supply and reduced sea-ice influence (Kjellman et al., 2020), the latter documented in both local and regional records, in Isfjorden and Fram Strait (Fig. 7D-E; Müller et al., 2012a, b and Rasmussen et al., 2012). Thus, we infer that ca. 8,200-7,300 cal. yrs B.P., due to these boundary conditions, Dunsappietjørna repeatedly approached carbonate supersaturation during the open-water and melt seasons, with runoff likely delivering hardwater enriched in ions from the local bedrock (Brekke and Hansson, 1990; Dallmann, 2015). This mechanism is consistent with Ca and bicarbonate (HCO_3) enrichment reported in the hydrochemistry of Tundra Lakes and is associated with solute delivery during seasonal runoff (Mazurek et al., 2012). It further meets the expectation that increased precipitation (including winter snowfall) can amplify melt-season

462 runoff and discharge signals in lacustrine archives (Auer et al., 2025). It also remains consistent
463 with leaf-wax hydrogen isotope (δ^2H) evidence for generally warm but unstable regional
464 hydroclimate between ca. 9,500-7,500 cal. yrs B.P. (Balascio et al., 2018), along with winter-
465 dominated precipitation persisting until ca. 6,000 cal. yrs B.P. (Kjellman et al., 2020).
466
467 Underlined by ~5 cm thick vegetation mat, unit 2 spans 91.5-54.5 cm and covers most of the
468 Mid- Holocene, from ca. 7,000 to 4,500 cal. yrs B.P (Figs. 2B and 3). SAR drops markedly
469 relative to unit 3 (Fig. 2B), and the sediments record a shift toward higher clastic delivery
470 superimposed on an authigenic carbonate component. We also report a drop in organic content,
471 suggesting a stepwise shortening of the open-water season. This shift is coeval with the end of
472 the first major Mid-Holocene cooling, terminating ca. 7,000 cal. yrs B.P. (van der Bilt et al.,
473 2018a), then the onset of progressive temperature decline from ca. 6,500 cal. yrs B.P. (Kong et
474 al., 2025). While other regional studies note prevailing ice-distal conditions in much of the Mid-
475 Holocene (Farnsworth et al., 2020), local multiproxy fjord evidence indicates renewed glacial
476 influence in Sassen- and Tempelfjorden, including the growth of Tunabreen between ca. 6,000
477 and 4,000 cal. yrs B.P. (Forwick et al., 2010). In parallel, progressive cooling is reflected by a
478 steady increase in ice rafting and seasonal sea-ice influence, both locally in Isfjorden and in
479 Fram Strait (Fig. 7D-E; Müller et al., 2012a, b and Rasmussen et al., 2012), shortening the
480 open-water season and reducing the duration of in-lake carbonate precipitation. In DST-2023-
481 GC, the growing input of Ti- and Fe-rich phases in the EM 3 grain-size window matches CS 2
482 from the Western alluvial plain (Figs. 3B-C, 5F-H and Tables S3-4). We also note that although
483 laminae are less frequent, they are thicker, and the authigenic clr Ca component remains within
484 a similar range to that in unit 3 (Fig. 3), as SEM imagery and SEM-EDS show flake-like,
485 anhedral authigenic carbonates in the unit's samples (Fig. 5A), similar to those reported in
486 Mazurek et al. (2012). We infer that hardwater enrichment and seasonal in-lake carbonate

precipitation likely persisted as in unit 3, sustained by continued solute delivery from carbonate weathering during melt-season runoff, but became diluted by rising Fe-Ti-rich minerogenic input from the West. This suggests that the shift from unit 3 to unit 2 reflects not the disappearance of carbonate precipitation but rather a growing detrital overprint under cooler, increasingly ice-affected conditions. We also note that the early part of unit 2, ca. 7,000-6,000 cal. yrs B.P. overlaps with winter-precipitation dominance inferred from δ^2H data (Kjellman et al., 2020), after which the seasonality signal becomes less clear.

Unit 1 comprises the uppermost 54.5-2.5 cm of the record, is divided into two subunits: 1b and 1a, and is overlain by a modern ~2.5 cm-thick vegetation mat (Fig. 3). Spanning the last ca. 4,500 yrs, it covers the end of the Mid- and the entirety of the Late Holocene (Fig. 2A). Sedimentation in Dunsappietjørna becomes progressively more detrital, coinciding with the second alkenone-inferred cooling step ca. 4,400-4,300 cal. yrs B.P. (van der Bilt et al., 2018a), followed by regional Neoglacial cooling (from ca. 4,200 cal. yrs B.P. onwards; Fig. 7F; van der Bilt et al., 2018a; Kong et al., 2025), and renewed glacier activity on Svalbard (Farnsworth et al., 2020). Unit 1 sediments are the darkest and, following an initial drop in density and clr Ti and Fe, show a sustained increase coupled with grain coarsening, contrasted by a steady LOI decline and generally lower clr Ca for most of the sequence (Figs. 3B-C and S4B). However, while initially dominated by EM 3 associated with clastic input from the West, EM 2 progressively increases and dominates the upper part of 1b and the entire 1a (Figs. 3B and S4B). A similar increase is observed in clr Ca. Moreover, from ca. 1,200 cal. yrs B.P., it broadly coincides with the onset of peak glacial activity in the region (Farnsworth et al., 2020), and is coeval with a decrease in clr Ti-Fe, as expressed by dense, light-beige lamination and a low rise in SAR (Figs. 2B and 3). Unlike in unit 3, this Ca peak is not accompanied by elevated LOI or EM 1 (Figs. 3B and S4B), suggesting it does not reflect renewed dominance of in-lake

hardwater precipitation. SEM imagery and SEM-EDS reveal slightly rounded, subhedral dolomite and calcite crystals in both core material and CS 1 samples (Figs. 5C-D, S6A-B, and Table S3), hinting at growing fluvial delivery of carbonate-bearing medium-silt from the seasonal Eastern inlet draining the Aitkenfjellen and Dalkallen side of the catchment during summer snowmelt and rainfall-driven runoff (Figs. 1D and S1C). The uppermost sequences of the core also overlap with more icy conditions in Isfjorden and increased sea-ice influence in Fram Strait (Fig. 7D-E; Müller et al., 2012a, b and Rasmussen et al., 2012). Overall, the clastic nature of unit 1 is consistent with Neoglacial boundary conditions that reduce authigenic in-lake production due to a shorter open-water window, while enhancing the contribution of minerogenic input from both Western and Eastern sources.

4.3. Mid- to Late Holocene Westerly wind input

The nearest largest mapped Fe- and Ti-rich lithologies are dolerite outcrops located West and Northwest of the lake, in Gåsøyane, Gipshuksletta, and Kapp Thordsen (see also Fig. 1C, and 'Study area'; NPI Geological maps, 2026; Brekke and Hansson, 1990; Nejbert et al., 2011; Senger et al., 2014; A. M. R. Sartell – personal communication). Out of the selected SEM-EDS oxide compositions of Fe-Ti-rich clasts within the $\pm 2\sigma$ grain-size window of EM 3, 69% (41 out of 59 spectra) yielded dolerite-indicative compositions, defined here as spectra that fall within or closely overlap the published major-oxide compositions reported for dolerites from Kapp Thordsen (CS-23) and Gåsøyane (CS-24; Nejbert et al., 2011), supporting a local dolerite source for the targeted clasts (see also our 'Methods'). Additional dolerite-indicative spectra not illustrated in Fig. 5 (and Table S3) are listed in Table S4.

RSL reconstructions from inner Isfjorden show rapid postglacial emergence from the marine limit, followed by a deceleration in the RSL fall after ca. 8,000-7,000 cal. yrs B.P. (Fig. 2C; see also 4.1; Strzelecki et al., 2026). Combined with the local topography (Fig. 1C), these reconstructions indicate that the dolerite outcrops around Gåsøyane, Gipshuksletta and Kapp Thordsen were at least partly emergent and therefore available as subaerial sources throughout the deposition of our record (Fig. 6A-B). Using the data from Bjonasletta beach-ridge system as a local analogue, RSL at ca. 8,000 cal. yrs B.P. was ~22 m a.s.l. (Fig. 2C; Strzelecki et al., 2026). This implies that ~51.9% of the mapped dolerite outcrop area in Gåsøyane and Gipshuksletta, and ~13.6% when including Kapp Thordsen, could be submerged at that time (Fig. 6B and Table S5). Thus, the availability of dolerite-derived material likely increased as RSL fell, particularly during the early part of the record (Figs. 2C and 6B). This time-varying exposure possibly explains the strength of the Fe-Ti-rich signal and, apart from the factors discussed in section 4.2.1, is a probable reason for the lower clr Ti-Fe values in older unit 3 (see also 'Supplementary Note 3').

Local dolerite outcrops lie upwind of Dunsappietjørna under the dominant summer Westerlies (Fig. 1B and Study area), consistent with reported valley-fjord wind channelling between the study area and the Sassenfjorden sector (Frank et al., 2023a, b). Accordingly, we interpret variability in EM 3 and its co-variation with clr Fe and Ti, captured by PC 1 (Fig. 4), as reflecting changes in Westerly-driven eolian input from the local dolerite outcrops. In periglacial settings, the expression of an eolian input is further controlled by seasonal cryospheric barriers (snow, frozen ground, lake ice) that regulate the availability and mobility of loose material for transport (Rasmussen et al., 2023; Rymer et al., 2022; Stachowska et al., 2024). At our site, the ice-free season is ~3 months-long per year (see also 'Study area'), but reported dust mobilisation windows in Svalbard range from summer to late autumn-early winter

(Kavan et al., 2020; Meinander et al., 2022; Rasmussen et al., 2023; Rymer et al., 2022). Nevertheless, local observations of dust deposition in Petuniabukta (Central Svalbard) show that the largest dust events are commonly associated with the warm season, when surface sediments are both snow-free and dry (Kavan et al., 2020). For quartz-density particles matching the EM 3 mode and the targeted Ti-Fe grains (see section 4.2.1), the initiation of motion remains threshold-limited, and it cannot be readily assessed as a simple linear wind-speed threshold. Coarse-silt often enters short-term suspension upon release, but this emission is usually caused by saltation impacts and sandblasting rather than by direct aerodynamic lift, as cohesion prevents the direct entrainment of fine particles (Kok et al., 2012). Moreover, effective mobilisation also depends strongly on surface moisture and the availability of saltating coarser grains that can release finer fractions by sandblasting (Fécan et al., 1999; Kok et al., 2012). Consequently, while we treat the variability captured by clr Fe-Ti and EM 3 as mainly an ice-free, summer Westerly signal, its intensity and timing probably reflect the past frequency of events that exceeded average seasonal thresholds and were further influenced by surface conditions (dryness, sediment cohesion, and supply). We also cannot entirely rule out occasional transport outside the peak summer season.

In this study, clr Fe has the strongest loading on PC 1 (Fig. 4 and Table S1), and is a diagnostic component of dolerite-derived input. Therefore, we selected it as the primary high-resolution proxy for summer Westerlies. We standardised clr Fe values to z-scores per unit and subunit to assess variability while accounting for sedimentological and geochemical differences across units (Toonen et al., 2015), particularly the non-stationary strength of dolerite-derived clasts. To identify phases of intensified eolian activity, we highlighted all values at or above the 90th percentile (*p90*) threshold (Hobday et al., 2016; Perkins-Kirkpatrick and Lewis, 2020), calculated separately for each unit or subunit, accounting for unit- and subunit-specific

backgrounds (Figs. 7C and S7). While this eliminates baseline offsets caused by lithology and time-varying source exposure, we interpret the resulting maxima as relative phases of intensified Westerly winds rather than discrete events. This is also because the record predates instrumental wind observations, and long archives often exhibit centennial-level chronological uncertainties (Kylander et al., 2023; Stachowska et al., 2024), as reflected here by a mean 2σ uncertainty of ca. 733 years (Figs. 2A, 7C, and S7). Clustering neighbouring maxima separated by <400 yrs (more than a half of the mean 2σ uncertainty), we identify four Mid- and Late Holocene phases of enhanced Westerly activity in the Dunsappietjørna archive between ca. 8,000-7,300 (phase I), 6,900-5,700 (phase II), 4,900-3,600 (phase III) and 1,200-1,000 (phase IV) cal. yrs B.P. (Figs. 7C and S7).

4.4. The Mid- and Late Holocene drivers of Westerly change

Although broadly overlapping with the progressive cooling, unlike major shifts in sedimentation, the four (I-IV) phases of Westerly maxima identified in our record are generally not monotonic with Svalbard climate transitions (Fig. 7B-F), and the wind signal remains comparatively stable through the recorded ca. 8,200 yrs. To contextualise major wind phases in terms of boundary conditions that control or modulate sediment entrainment and deposition, we compare them to local (Isfjorden) and regional Holocene-long records that resolve multi-centennial variability in temperature, ice rafting, sea-ice, and glacial history. We do not treat these variables as direct controls on wind strength but rather as boundary conditions that influence near-surface stress, open-water exposure (Frank et al., 2025), sediment availability, and the efficiency with which winds translate into eolian transport (Stachowska et al., 2024). Accordingly, phase I (ca. 8,000-7,300 cal. yrs B.P.; Fig. 7C) occurs under an optimal but transitional early Mid- Holocene background (Fig. 7F; Kong et al., 2025 and van der Bilt et al.,

2018a), aligning with the regional glacier minimum ca. 8,000-6,000 cal. yrs B.P. (Farnsworth et al., 2020), yet also partly overlapping with the first major Mid- Holocene cooling step ca. 7,800-7,000 cal. yrs B.P. (van der Bilt et al., 2018a). This interval of enhanced wind activity in the study area also falls within stepwise cooling in Isfjorden, ca. 8,200 and 7,400 cal. yrs B.P., linked to increased ice rafting, polar-water influence and seasonal sea-ice (Fig. 7D; Rasmussen et al., 2012), as well as more persistent sea-ice conditions in the region, as shown by the Fram Strait record (Fig. 7E; Müller et al., 2012a, b). This local progressive reduction in open-water conditions is also consistent with a slowing in beach-ridge formation (Strzelecki et al., 2026). Phase II (ca. 6,900-5,700 cal. yrs B.P.) is coeval with the onset of the regional cooling trend (van der Bilt et al., 2018a; Kong et al., 2025), particularly from ca. 6,500 cal. yrs B.P. (Kong et al., 2025), although following the end of the glacier minimum cal. 8,000 cal. yrs B.P., Farnsworth et al. (2020) report uneven regional constraints on glacier conditions until ca. 4,500 cal. yrs B.P., contrasted by the growth of local Tunabreen between ca. 6,000-4,000 cal. yrs B.P. (Forwick et al., 2010). Similar to phase I, our second phase of Westerly maxima is coeval with the increasing ice rafting and sea-ice influence (Müller et al., 2012a, b; Rasmussen et al., 2012), and with a further drop in the Bjonasletta's beach-ridge progradation (Strzelecki et al., 2026). Both phases I-II are therefore expressed despite an evolving polar-water regime, consistent with the interpretation that the warm-season Westerly signal can peak under both relatively mild and progressively cooler backgrounds. Phase III (ca. 4,900-3,600 cal. yrs B.P.) shows that enhanced Westerly input overlaps the second major alkenone-inferred Mid- Holocene cooling step, ca. 4,400-4,300 cal. yrs B.P. (van der Bilt et al., 2018a), then spans the Neoglacial (from ca. 4,200 cal. yrs B.P.), and the onset of episodic glacier expansion after ca. 4,000 cal. yrs B.P. (Farnsworth et al., 2020). It is also in phase with the stepwise cooling in Isfjorden that precedes minimum bottom-water temperatures between ca. 4,000 and 2,000 cal. yrs B.P. under strengthened polar water and sea-ice influence (Rasmussen et al., 2012), reducing wave

exposure and further slowing the beach-ridge progradation (Strzelecki et al., 2026). Local fjord studies further suggest glacier advances around Sassen- and Tempelfjorden coeval with phase III (Forwick et al., 2010). Phase IV (ca. 1,200-1,000 cal. yrs B.P.) occurs within the cold Late Holocene mean state marked by a further drop in spring and summer temperatures (van der Bilt et al., 2018a; Kong et al., 2025), with enhanced wind activity shortly overlapping with the regional peak glacier activity ca. 1,000-500 cal. yrs. B.P. (Farnsworth et al., 2020). However, while regional records suggest increased sea-ice cover (Müller et al., 2012a, b), the Isfjorden shows progressively less stable bottom-water conditions following episodic warmer Atlantic Water (AW) inflows after ca. 2,000 cal. yrs B.P. (Rasmussen et al., 2012). Forwick et al. (2010) also document local heterogeneity through multiple glacier-front advances and retreats over the past two millennia. Overall, our record does not show additional sustained clusters of Westerly maxima through much of the Late Holocene, between ca. 3,600-1,200 and after ca. 1,000 cal. yrs B.P. (Figs. 7C and S7). This suggests reduced clastic input under colder, generally more ice-affected boundary conditions in which longer seasonal ice cover and stronger cryogenic barriers shorten the effective depositional window, and more persistent sea-ice reduces near-surface coupling and open-water exposure. At the same time, we again emphasise that our Westerly maxima do not show a monotonic response to climate shifts, as none of the several milder episodes associated with AW inflows into Isfjorden in the last two millennia is accompanied by values exceeding the *p90* threshold (Fig. 7C-D; Rasmussen et al., 2012). Taken together, we infer that in the DST-2023 GC record, the depositional expression of Westerlies depended on the interaction of atmospheric forcing with changing exposure, cryogenic barriers, and sediment availability.

To place the Dunsappietjørna record into a broader Svalbard paleo wind context, we compare it with the Steinbruvatnet record from Southern Svalbard (Fig. 7B-C; Stachowska et al., 2024).

Both lacustrine archives isolate multi-centennial variability in warm-season clastic input attributed to the Westerlies and are reconstructed using comparable high-resolution multiproxy methods (Stachowska et al., 2024). However, the Southern Svalbard record resolves the wind maxima between ca. 9,700 and 1,700 cal. yrs B.P. (Stachowska et al., 2024), whereas Dunsappietjørna – although lacking the Early Holocene context – extends High Arctic Westerly wind behaviour to the present. Beyond the difference in temporal coverage, there is a fundamental contrast in setting: while Dunsappietjørna lies in an inner-fjord environment, Steinbruvatnet is located in an exposed coastal sector, capturing a more direct expression of ocean-atmosphere dynamics in the North Atlantic (Stachowska et al., 2024). We note that the similarity between Westerly maxima in the Central and Southern Svalbard records is observable only between ca. 8,200 and 5,700 cal. yrs B.P. (phases I-II of our record, Fig. 7B-C), with little overall correspondence thereafter. Chronological offsets are plausible because both archives exhibit centennial-scale age uncertainties (Stachowska et al., 2024). Moreover, misalignments are expected in multi-centennial storm reconstructions – with storminess here defined as wind strength and wave height after Stachowska et al. (2024) – because proxy and site responses can diverge even when shifts in storminess are broadly similar, including variability within a sequence and across a wider (~100 km) transect (Kylander et al., 2023). Kylander et al. (2023) further argue that lateral shifts in storm track position can result in strong spatial gradients, with sites adjacent to the storm track responding differently from those at its margins.

Although paleo data are limited in the study area, modern wind observations reveal considerable spatial heterogeneity in both surface wind direction and magnitude relative to the open coast, as shown in Fig. S8 (Frank et al., 2023a, b, 2025; MET Norway, 2026). These patterns are largely driven by valley-fjord orientation, headland speed-up zones, and land-sea thermal contrast (Frank et al., 2023a, b, 2025). The closest available inner-fjord observations for our

study area are from the Isfjorden-Gåsøyane station, which began full operations only in 2025 (MET Norway, 2026). Such a short record cannot resolve longer-term trends and only hints at a seasonal cycle in wind direction and strength. Nevertheless, in 2025, Westerly winds (SW, WSW, W, WNW, NW) accounted for ~21% of annual observations, peaking at ~63% of all measured winds in July and of maximum gale speed (≤17.1 m/s). The JJA wind roses from other Isfjorden stations further show that directional regimes and high-wind classes vary strongly across the fjord system (Fig. S8; MET Norway, 2026), consistent with local topographic steering, as highlighted by Frank et al. (2025). At Gåsøyane, Southwest-Northwest winds account for ~39.4% of JJA observations, but winds of ≥10.7 m/s speed (fresh breeze or stronger) are more frequent from North-Northeast and East-Southeast than from Western-Northwestern directions. Further air-sea measurements by Frank et al. (2025) suggest that in Isfjorden, sea-ice conditions play a first-order control on near-surface air-sea coupling and on the efficiency with which winds are expressed over open-water, and show that even modest sea-ice can reduce the air-sea temperature contrast and shorten open-water exposure, weakening surface winds despite potentially strong flow aloft. This sensitivity is also consistent with observations showing that surface drag can peak at intermediate sea-ice concentrations due to form drag from floe edges, and is strongly dependent on ice morphology and floe size (Elvidge et al., 2016; Lüpkes and Birnbaum, 2005).

As previously mentioned in section 4.3, a further implication is that the delivery of EM 3-sized (coarse-silt) eolian fraction could likely be disproportionately influenced by episodic high-wind events associated with cyclones passing over the archipelago, rather than by average background wind flow. In the modern Arctic, summer cyclones can be linked to brief periods of extreme near-surface winds and increased surface wind stress, including that over sea-ice (Croad et al., 2023; Tanaka et al., 2012). Preferred cyclone track corridors and cyclone types

711 can also impose spatial gradients in cyclone occurrence and intensity, as well as in associated
712 wind extremes (Croad et al., 2023). Because Arctic cyclone behaviour is linked to the
713 distribution of lower-tropospheric temperature gradients and sea-ice extent (Simmonds and
714 Rudeva, 2014), Holocene changes in insolation and boundary conditions at the ocean-ice
715 margin can plausibly modulate storm track positions and pathways in the North Atlantic (Orme
716 et al., 2017). Case observations from Fram Strait show that cyclones generated at the marginal
717 ice zone can propagate NNE along the ice edge and produce short-lived (several-hour) winds
718 exceeding 20 m/s (Brümmer et al., 2003). On the other hand, even when winds ≥20 m/s are
719 treated as a practical indicator of Arctic cyclone-strength winds, following Fram Strait
720 observations by Brümmer et al. (2003), wind rose data provide little direct support for such a
721 regime within Isfjorden (Fig. S8). This is also consistent with other modern observations from
722 Western Spitsbergen showing that wind-speed extremes depend strongly on circulation, with
723 the largest positive wind-speed anomalies occurring during Southwestern-Southern air-mass
724 advection (Araźny et al., 2022). At the same time, summertime (JJA) winds of ≥10.7 m/s occur
725 at several Isfjorden stations, including Gåsøyane, suggesting that threshold-exceeding winds
726 may be a realistic modern analogue for coarse-silt mobilisation even in the absence of a clear
727 cyclone-strength signal. In that framework, we cannot dismiss the possibility that small shifts
728 in past cyclone or storm track positions may still have altered the frequency of winds exceeding
729 entrainment thresholds that can mobilise coarse-silt, thereby influencing the variability of the
730 Fe-Ti-rich dolerite-derived input. At the same time, we want to emphasise that the data do not
731 justify directly identifying the observed JJA high-wind regimes in the study area with cyclones.
732
733 Overall, we use modern observations to evaluate the plausibility of wind steering and exposure
734 contrasts, and interpret the transfer of regional circulation variability to eolian sediment delivery
735 as nonlinear and highly site-dependent in inner-fjord settings. This approach aligns with the

limited correlation with Steinbruvatnet outside phases I-II (Stachowska et al., 2024), the plausibility of centennial-scale chronological offsets (Kylander et al., 2023), and the expectation that coarse-silt delivery responds disproportionately to wind events exceeding the grain entrainment threshold. We also acknowledge that the expression of these patterns likely varied throughout the Mid- and Late Holocene. Accordingly, the Dunsappietjørna archive is most likely locally filtered due to valley-fjord wind steering, a sea-ice-limited fetch and exposure, and time-varying sediment availability and deposition. If true, this may explain why our inner-valley-fjord setting does not directly reflect the open-coastal patterns of increased wind activity during regional cooling phases (Stachowska et al., 2024), and why major regional transitions might either not be shown or are highly muted or phase-shifted. However, our record also does not support the view that a warmer, less icy Arctic will be stormier due to stronger surface winds, longer fetch, and enhanced wave activity (Casas-Prat and Wang, 2020; Li et al., 2019; Mioduszewski et al., 2018). Instead, Dunsappietjørna provides a high-resolution inner-fjord perspective on High Arctic eolian variability over the last ca. 8,200 yrs and reinforces the need for spatial transects and multi-site comparisons when synthesising storm reconstructions across Svalbard.

5. Conclusions

This study shows that inner-fjord lake sediments can preserve a high-resolution eolian record over centennial timescales, provided that local topographic filtering and complex boundary conditions are systematically accounted for. Our results suggest that isolating eolian signals in such settings is most effective when employing an integrated multiproxy toolbox that couples high-resolution core scanning with grain-specific provenance validation.

761 The primary contribution of this work is the application of a workflow that bridges macro-scale
762 stratigraphy and micro-scale mineralogy. By integrating XRF and CT scanning with End
763 Member Modelling Analysis (EMMA), we identify a coarse-silt component indicative of wind-
764 driven transport. Critically, we validate this eolian signal using Scanning Electron Microscopy
765 and Energy Dispersive X-ray Spectroscopy (SEM-EDS) to map and geochemically fingerprint
766 Fe-Ti-rich minerogenic phases. This allows us to link the sediment to specific dolerite outcrops
767 located West of the basin, providing a diagnostic provenance target that distinguishes eolian
768 clastic input from other parallel depositional processes.
769
770 Applying this toolbox to Dunsappietjørna, we resolve four multi-centennial phases of enhanced
771 eolian activity over the past ca. 8,200 yrs, and show how inner-fjord-valley geometry and time-
772 varying sediment availability modulate the regional atmospheric signal. Our findings indicate
773 that while Dunsappietjørna likely captures broader Holocene wind trends, the magnitude of the
774 depositional response in this sheltered inner-fjord setting is heavily filtered by local boundary
775 conditions and sediment supply. Accordingly, the record does not support a simple monotonic
776 relationship between either colder or warmer conditions and stronger winds at this site.
777
778 On a regional scale, the scarcity and varied sensitivity of Arctic wind archives make direct
779 comparisons challenging. To improve the comparability of these records, we advocate for the
780 wider adoption of this provenance-validated workflow. Future research should apply this
781 multiproxy approach along spatial transects – from exposed coastal sites to sheltered inner-fjord
782 valleys – to better constrain how complex topography filters atmospheric forcing, as we believe
783 that such high-resolution, validated archives are essential for understanding how Arctic
784 warming will continue to reshape wind patterns, sea-ice extent, and post-glacial sediment
785 dynamics.

786

787 **Acknowledgements**

788

789 This research received funding from the Polish National Science Centre (NCN) grant *ASPIRE*
790 *– Arctic storm impacts recorded in beach-ridges and lake archives: scenarios for less icy future*
791 (No. UMO-2020/37/B/ST10/03074), led by M.C.S. (PI) and W.v.d.B. (Co-PI). W.v.d.B.'s
792 contribution was additionally supported by a *Starting Grant* from the Trond Mohn Research
793 Foundation (TMF; No. TMS2021STG01). In 2024, Z.S. received a mobility grant from *HarSval*
794 *Bilateral initiative aiming at a Harmonisation of the Svalbard cooperation and activities*
795 *funding from the means of the EEA and Norway Grants 2014-2021* (No. UMO-
796 2023/43/7/ST10/00001), as well as the Doctoral School of the University of Szczecin's Grant
797 for scientific development, which both supported her mobility to Bergen and Longyearbyen. In
798 2025, Z.S.'s research activity was further supported by the Ministry of Science and Higher
799 Education's *Regional Excellence Initiative Programme* (No. 3/D/2025) and the Foundation for
800 Polish Science (FNP) *Start Programme*. We sincerely thank Andreea G. Auer (A.G.A.) for
801 sharing her expertise in multivariate statistics. We also thank Irene Heggstad for dedicating her
802 time and knowledge to Scanning Electron Microscopy (SEM) and Energy-Dispersive X-ray
803 Spectroscopy (SEM-EDS), as well as for assisting with additional technical questions. For the
804 latter, we are also grateful to Harald Hausen. Our thanks go to Haflidi Haflidason for his
805 feedback on the stratigraphy and for his tips on mapping dolerite clasts using SEM and SEM-
806 EDS. We also appreciate Danuta Cembrowska-Lech for providing polycarbonate membranes
807 and for advice on their use in sample preparation. We thank Jan Magne Cederstrøm for
808 performing the Computed Tomography (CT) scan and providing his recommendations to
809 correct the compressed CT grayscale values. We express our gratitude to Pål T. Mørkved for
810 granting access to the weighing room and microbalance in the Facility for advanced isotopic

research and monitoring of weather, climate and biogeochemical cycling (FARLAB) at the University of Bergen, which helped us assess the most stable readings of radiocarbon samples. We extend our sincere appreciation to Kim Senger and Anna M. R. Sartell for sharing data and their expertise in mineralogy and petrography of local dolerites. Lastly, we thank all our colleagues who, along with A.G.A., participated in the fieldwork: Chris Hein, Sebastian Lindhorst, Joseph M. Buckby, Knut I. L. Tveit, and Peter Betlem.

Author contributions statement

W.v.d.B. and M.C.S. secured funding for this study. The study design and methodology were primarily developed by W.v.d.B. and implemented by Z.S., with contributions from I.H.T., W.v.d.B., M.C.S., J.K., and M.F.A.F. W.v.d.B., M.C.S., J.K., Z.S., and M.F.A.F. participated in the fieldwork and conducted sediment sampling. Z.S. wrote the original draft, and all authors contributed to its final version. Figures were produced by Z.S. and J.K.

Competing Interests statement

The authors declare no competing interests.

Data availability

The authors declare that all data generated from the sediment core DST-2023 GC for this study, and presented in its figures and tables (including the Supplementary Information file), have

been made available in the DataverseNO repository, where the files can be accessed under the following link: doi:10.18710/K3CDJJ. Source data generated in this study are also provided with this paper as an .xls file, with a separate sheet for each figure and table.

References

Araźny, A., Przybylak, R., and Kejna, M.: The Influence of Atmospheric Circulation on Mean and Extreme Weather Conditions on Kaffiøyra (NW Spitsbergen, Svalbard Archipelago) in the Summer Seasons 1975–2015, Front. Environ. Sci., 10, 867106, https://doi.org/10.3389/fenvs.2022.867106, 2022.

Auer, A. G., Van Der Bilt, W. G. M., Schomacker, A., Bakke, J., Støren, E. W. N., Buckby, J. M., Cederstrøm, J. M., and Van Der Plas, S.: Hydroclimate intensification likely aided glacier survival on Svalbard in the Early Holocene, Commun Earth Environ, 6, 100, https://doi.org/10.1038/s43247-025-02064-z, 2025.

Balascio, N. L., D'Andrea, W. J., Gjerde, M., and Bakke, J.: Hydroclimate variability of High Arctic Svalbard during the Holocene inferred from hydrogen isotopes of leaf waxes, Quaternary Science Reviews, 183, 177–187, https://doi.org/10.1016/j.quascirev.2016.11.036, 2018.

Bertrand, S., Tjallingii, R., Kylander, M. E., Wilhelm, B., Roberts, S. J., Arnaud, F., Brown, E., and Bindler, R.: Inorganic geochemistry of lake sediments: A review of analytical techniques and guidelines for data interpretation, Earth-Science Reviews, 249, 104639, https://doi.org/10.1016/j.earscirev.2023.104639, 2024.

van der Bilt, W. G. M., D'Andrea, W. J., Bakke, J., Balascio, N. L., Werner, J. P., Gjerde, M., and Bradley, R. S.: Alkenone-based reconstructions reveal four-phase Holocene temperature evolution for High Arctic Svalbard, Quaternary Science Reviews, 183, 204–213, https://doi.org/10.1016/j.quascirev.2016.10.006, 2018a.

van der Bilt, W. G. M., Rea, B., Spagnolo, M., Roerdink, D. L., Jørgensen, S. L., and Bakke, J.: Novel sedimentological fingerprints link shifting depositional processes to Holocene climate transitions in East Greenland, Global and Planetary Change, 164, 52–64, https://doi.org/10.1016/j.gloplacha.2018.03.007, 2018b.

van der Bilt, W. G. M., D'Andrea, W. J., Werner, J. P., and Bakke, J.: Early Holocene Temperature Oscillations Exceed Amplitude of Observed and Projected Warming in Svalbard Lakes, Geophysical Research Letters, 46, 14732–14741, https://doi.org/10.1029/2019GL084384, 2019.

Blaauw, M., Christen [aut, J. A., ctb, cph, Lopez, M. A. A., Vazquez, J. E., V, O. M. G., Belding, T., Theiler, J., Gough, B., and Karney, C.: rbacon: Age-Depth Modelling using Bayesian Statistics, 2022.

Blott, S. J. and Pye, K.: GRADISTAT: a grain size distribution and statistics package for the analysis of unconsolidated sediments, Earth Surf. Process. Landforms, 26, 1237–1248, https://doi.org/10.1002/esp.261, 2001.

Brekke, B. and Hansson, R.: Environmental atlas Gipsdalen, Svalbard. Vol. II, Reports on the quaternary geology, vegetation, flora, and fauna of Gipsdalen, and the marine ecology of Gipsvika, 1990.

Brooks, R. A. and Di Chiro, G.: Statistical limitations in x-ray reconstructive tomography, Medical Physics, 3, 237–240, https://doi.org/10.1118/1.594240, 1976.

879 Brümmer, B., Müller, G., and Hoeber, H.: A Fram Strait cyclone: Properties and impact on
880 ice drift as measured by aircraft and buoys, J. Geophys. Res., 108, 2002JD002638,
881 https://doi.org/10.1029/2002JD002638, 2003.

882 Casas-Prat, M. and Wang, X. L.: Projections of Extreme Ocean Waves in the Arctic and
883 Potential Implications for Coastal Inundation and Erosion, JGR Oceans, 125,
884 e2019JC015745, https://doi.org/10.1029/2019JC015745, 2020.

885 Chen, W. and Guillaume, M.: HALS-based NMF with flexible constraints for hyperspectral
886 unmixing, EURASIP J. Adv. Signal Process., 2012, 54, https://doi.org/10.1186/1687-6180-
887 2012-54, 2012.

888 Cnudde, V. and Boone, M. N.: High-resolution X-ray computed tomography in geosciences:
889 A review of the current technology and applications, Earth-Science Reviews, 123, 1–17,
890 https://doi.org/10.1016/j.earscirev.2013.04.003, 2013.

891 Cox Analytical System: Itrax Core Scanner: Q-Spec 6.5.2. Software Manual. Mölndal, 13 pp,
892 2008.

893 Croad, H. L., Methven, J., Harvey, B., Keeley, S. P. E., Volonté, A., and Hodges, K. I.: A
894 Climatology of Summer-Time Arctic Cyclones Using a Modified Phase Space, Geophysical
895 Research Letters, 50, e2023GL105993, https://doi.org/10.1029/2023GL105993, 2023.

896 Dallmann, W. K.: Geoscience atlas of Svalbard, Norsk Polarinstitutt, 2015.

897 Davies, S. J., Lamb, H. F., and Roberts, S. J.: Micro-XRF Core Scanning in Palaeolimnology:
898 Recent Developments, in: Micro-XRF Studies of Sediment Cores: Applications of a non-
899 destructive tool for the environmental sciences, edited by: Croudace, I. W. and Rothwell, R.

900 G., Springer Netherlands, Dordrecht, 189–226, https://doi.org/10.1007/978-94-017-9849-5_7,
901 2015.

902 Dietze, M., Schulte, P., and Dietze, E.: Application of end-member modelling to grain-size
903 data: Constraints and limitations, Sedimentology, 69, 845–863,
904 https://doi.org/10.1111/sed.12929, 2022.

905 Elvidge, A. D., Renfrew, I. A., Weiss, A. I., Brooks, I. M., Lachlan-Cope, T. A., and King, J.
906 C.: Observations of surface momentum exchange over the marginal ice zone and
907 recommendations for its parametrisation, Atmos. Chem. Phys., 16, 1545–1563,
908 https://doi.org/10.5194/acp-16-1545-2016, 2016.

909 Farnsworth, W. R., Allaart, L., Ingólfsson, Ó., Alexanderson, H., Forwick, M., Noormets, R.,
910 Retelle, M., and Schomacker, A.: Holocene glacial history of Svalbard: Status, perspectives
911 and challenges, Earth-Science Reviews, 208, 103249,
912 https://doi.org/10.1016/j.earscirev.2020.103249, 2020.

913 Fécan, F., Marticorena, B., and Bergametti, G.: Parametrization of the increase of the aeolian
914 erosion threshold wind friction velocity due to soil moisture for arid and semi-arid areas, Ann.
915 Geophys., 17, 149–157, https://doi.org/10.1007/s00585-999-0149-7, 1999.

916 Førland, E. J., Benestad, R., Hanssen-Bauer, I., Haugen, J. E., and Skaugen, T. E.:
917 Temperature and Precipitation Development at Svalbard 1900–2100, Advances in
918 Meteorology, 2011, 1–14, https://doi.org/10.1155/2011/893790, 2011.

919 Forman, S. L., Lubinski, D. J., Ingólfsson, Ó., Zeeberg, J. J., Snyder, J. A., Siegert, M. J., and
920 Matishov, G. G.: A review of postglacial emergence on Svalbard, Franz Josef Land and
921 Novaya Zemlya, northern Eurasia, Quaternary Science Reviews, 23, 1391–1434,
922 https://doi.org/10.1016/j.quascirev.2003.12.007, 2004.

923 Forwick, M., Vorren, T. O., Hald, M., Korsun, S., Roh, Y., Vogt, C., and Yoo, K.-C.: Spatial
924 and temporal influence of glaciers and rivers on the sedimentary environment in
925 Sassenfjorden and Tempelfjorden, Spitsbergen, SP, 344, 163–193,
926 https://doi.org/10.1144/SP344.13, 2010.

927 Frank, L., Jonassen, M. O., Skogseth, R., and Vihma, T.: Atmospheric Climatologies Over
928 Isfjorden, Svalbard, JGR Atmospheres, 128, e2022JD038011,
929 https://doi.org/10.1029/2022JD038011, 2023a.

930 Frank, L., Jonassen, M. O., and Remes, T.: IWIN: The Isfjorden Weather Information
931 Network, https://doi.org/10.21343/EBRW-W846, 2023b.

932 Frank, L., Jonassen, M. O., Skogseth, R., and Vihma, T.: Air–sea–ice interactions in
933 Isfjorden, Svalbard: An atmospheric perspective, Quart J Royal Meteoro Soc, 151, e4956,
934 https://doi.org/10.1002/qj.4956, 2025.

935 Goslar, T., Czernik, J., and Goslar, E.: Low-energy 14C AMS in Poznań Radiocarbon
936 Laboratory, Poland, Nuclear Instruments and Methods in Physics Research Section B: Beam
937 Interactions with Materials and Atoms, 223–224, 5–11,
938 https://doi.org/10.1016/j.nimb.2004.04.005, 2004.

939 Goslin, J. and Clemmensen, L. B.: Proxy records of Holocene storm events in coastal barrier
940 systems: Storm-wave induced markers, Quaternary Science Reviews, 174, 80–119,
941 https://doi.org/10.1016/j.quascirev.2017.08.026, 2017.

942 Hammer, O., Harper, D., and Ryan, P.: PAST: Paleontological Statistics Software Package for
943 Education and Data Analysis, Palaeontologia Electronica, 4, 1–9, 2001.

944 Hess, K., Engel, M., Patel, T., Vakhrameeva, P., Koutsodendris, A., Klemt, E., Hansteen, T.
945 H., Kempf, P., Dawson, S., Schön, I., and Heyvaert, V. M. A.: A 1500-year record of North
946 Atlantic storm flooding from lacustrine sediments, Shetland Islands (UK), J Quaternary
947 Science, jqs.3568, https://doi.org/10.1002/jqs.3568, 2023.

948 Hobday, A. J., Alexander, L. V., Perkins, S. E., Smale, D. A., Straub, S. C., Oliver, E. C. J.,
949 Benthuysen, J. A., Burrows, M. T., Donat, M. G., Feng, M., Holbrook, N. J., Moore, P. J.,
950 Scannell, H. A., Sen Gupta, A., and Wernberg, T.: A hierarchical approach to defining marine
951 heatwaves, Progress in Oceanography, 141, 227–238,
952 https://doi.org/10.1016/j.pocean.2015.12.014, 2016.

953 Itamiya, H., Sugita, R., and Sugai, T.: Analysis of the surface microtextures and morphologies
954 of beach quartz grains in Japan and implications for provenance research, Prog Earth Planet
955 Sci, 6, 43, https://doi.org/10.1186/s40645-019-0287-9, 2019.

956 Kavan, J., Láska, K., Nawrot, A., and Wawrzyniak, T.: High Latitude Dust Transport Altitude
957 Pattern Revealed from Deposition on Snow, Svalbard, Atmosphere, 11, 1318,
958 https://doi.org/10.3390/atmos11121318, 2020.

959 Kjellman, S. E., Schomacker, A., Thomas, E. K., Håkansson, L., Duboscq, S., Cluett, A. A.,
960 Farnsworth, W. R., Allaart, L., Cowling, O. C., McKay, N. P., Brynjólfsson, S., and
961 Ingólfsson, Ó.: Holocene precipitation seasonality in northern Svalbard: Influence of sea ice
962 and regional ocean surface conditions, Quaternary Science Reviews, 240, 106388,
963 https://doi.org/10.1016/j.quascirev.2020.106388, 2020.

964 Kok, J. F., Parteli, E. J. R., Michaels, T. I., and Karam, D. B.: The physics of wind-blown
965 sand and dust, Rep. Prog. Phys., 75, 106901, https://doi.org/10.1088/0034-
966 4885/75/10/106901, 2012.

967 Kong, S.-R., Van Der Bilt, W. G. M., Mørkved, P. T., Wörmer, L., Hasal, K., and D'Andrea,
968 W. J.: Sub-centennially resolved reconstruction of surface temperature on High Arctic
969 Svalbard for the past 13,000 years, Earth and Planetary Science Letters, 671, 119646,
970 https://doi.org/10.1016/j.epsl.2025.119646, 2025.

971 Element — Oxide Conversions: https://meteorites.wustl.edu/goodstuff/oxides.htm, last
972 access: 26 November 2023.

973 Kotov, S. and Pälike, H.: QAnalySeries – a cross-platform time series tuning and analysis
974 tool, Earth and Space Science Open Archive, https://doi.org/10.1002/essoar.10500226.1,
975 2018.

976 Kylander, M. E., Ampel, L., Wohlfarth, B., and Veres, D.: High-resolution X-ray
977 fluorescence core scanning analysis of Les Echets (France) sedimentary sequence: new
978 insights from chemical proxies: XRF CORE SCANNING ANALYSIS OF LES ECHETS
979 SEDIMENTARY SEQUENCE, J. Quaternary Sci., 26, 109–117,
980 https://doi.org/10.1002/jqs.1438, 2011.

981 Kylander, M. E., Martínez-Cortizas, A., Sjöström, J. K., Gåling, J., Gyllencreutz, R., Bindler,
982 R., Alexanderson, H., Schenk, F., Reinardy, B. T. I., Chandler, B. M. P., and Gallagher, K.:
983 Storm chasing: Tracking Holocene storminess in southern Sweden using mineral proxies from
984 inland and coastal peat bogs, Quaternary Science Reviews, 299, 107854,
985 https://doi.org/10.1016/j.quascirev.2022.107854, 2023.

986 Li, J., Ma, Y., Liu, Q., Zhang, W., and Guan, C.: Growth of wave height with retreating ice
987 cover in the Arctic, Cold Regions Science and Technology, 164, 102790,
988 https://doi.org/10.1016/j.coldregions.2019.102790, 2019.

989 Lulák, M., Nývlt, D., Novák, M., and Kavan, J.: Holocene relative sea level changes and their
990 consequences for the development of the palaeoshoreline in central Svalbard, Czech Polar
991 Rep., 15, 121–138, https://doi.org/10.5817/CPR2025-S-7, 2026.

992 Lüpkes, C. and Birnbaum, G.: 'Surface Drag in the Arctic Marginal Sea-ice Zone: A
993 Comparison of Different Parameterisation Concepts,' Boundary-Layer Meteorol, 117, 179–
994 211, https://doi.org/10.1007/s10546-005-1445-8, 2005.

995 Malvern Panalytical: Mastersizer 3000 User Manual English, 2015.

996 Marshall, J. R., Bull, P. A., and Morgan, R. M.: Energy regimes for aeolian sand grain surface
997 textures, Sedimentary Geology, 253–254, 17–24,
998 https://doi.org/10.1016/j.sedgeo.2012.01.001, 2012.

999 Mazurek, M., Paluszkiewicz, R., Rachlewicz, G., and Zwoliński, Z.: Variability of Water
1000 Chemistry in Tundra Lakes, Petuniabukta Coast, Central Spitsbergen, Svalbard, The
1001 Scientific World Journal, 2012, 1–13, https://doi.org/10.1100/2012/596516, 2012.

1002 Meinander, O., Dagsson-Waldhauserova, P., Amosov, P., Aseyeva, E., Atkins, C., Baklanov,
1003 A., Baldo, C., Barr, S. L., Barzycka, B., Benning, L. G., Cvetkovic, B., Enchilik, P., Frolov,
1004 D., Gassó, S., Kandler, K., Kasimov, N., Kavan, J., King, J., Koroleva, T., Krupskaya, V.,
1005 Kulmala, M., Kusiak, M., Lappalainen, H. K., Laska, M., Lasne, J., Lewandowski, M., Luks,
1006 B., McQuaid, J. B., Moroni, B., Murray, B., Möhler, O., Nawrot, A., Nickovic, S., O'Neill, N.
1007 T., Pejanovic, G., Popovicheva, O., Ranjbar, K., Romanias, M., Samonova, O., Sanchez-
1008 Marroquin, A., Schepanski, K., Semenkov, I., Sharapova, A., Shevnina, E., Shi, Z., Sofiev,
1009 M., Thevenet, F., Thorsteinsson, T., Timofeev, M., Umo, N. S., Uppstu, A., Urupina, D.,
1010 Varga, G., Werner, T., Arnalds, O., and Vukovic Vimic, A.: Newly identified climatically and

1011 environmentally significant high-latitude dust sources, Atmos. Chem. Phys., 22, 11889–
1012 11930, https://doi.org/10.5194/acp-22-11889-2022, 2022.

1013 MET Norway: https://seklima.met.no/, last access: 2 January 2026.

1014 Mioduszewski, J., Vavrus, S., and Wang, M.: Diminishing Arctic Sea Ice Promotes Stronger
1015 Surface Winds, J. Climate, 31, 8101–8119, https://doi.org/10.1175/JCLI-D-18-0109.1, 2018.

1016 Montgomery, D. C.: Design and Analysis of Experiments, John Wiley & Sons, 752 pp., 2017.

1017 Muilwijk, M., Hattermann, T., Martin, T., and Granskog, M. A.: Future sea ice weakening
1018 amplifies wind-driven trends in surface stress and Arctic Ocean spin-up, Nat Commun, 15,
1019 6889, https://doi.org/10.1038/s41467-024-50874-0, 2024.

1020 Müller, J., Werner, K., Stein, R., Fahl, K., Moros, M., and Jansen, E.: Age determinations,
1021 biomarker analyses, and accumulation rates of three sediment cores from the Fram Strait, 6
1022 datasets, https://doi.org/10.1594/PANGAEA.779628, 2012a.

1023 Müller, J., Werner, K., Stein, R., Fahl, K., Moros, M., and Jansen, E.: Holocene cooling
1024 culminates in sea ice oscillations in Fram Strait, Quaternary Science Reviews, 47, 1–14,
1025 https://doi.org/10.1016/j.quascirev.2012.04.024, 2012b.

1026 Nejbert, K., Krajewski, K. P., Dubinska, E., and Pécskay, Z.: Dolerites of Svalbard, north-
1027 west Barents Sea Shelf: age, tectonic setting and significance for geotectonic interpretation of
1028 the High-Arctic Large Igneous Province, Polar Research, 30, 7306,
1029 https://doi.org/10.3402/polar.v30i0.7306, 2011.

1030 Newbury, D. E. and Ritchie, N. W. M.: Performing elemental microanalysis with high
1031 accuracy and high precision by scanning electron microscopy/silicon drift detector energy-

1032 dispersive X-ray spectrometry (SEM/SDD-EDS), J Mater Sci, 50, 493–518,
1033 https://doi.org/10.1007/s10853-014-8685-2, 2015.

1034 Nordli, Ø., Wyszyński, P., Gjelten, H. M., Isaksen, K., Łupikasza, E., Niedźwiedź, T., and
1035 Przybylak, R.: Revisiting the extended Svalbard Airport monthly temperature series, and the
1036 compiled corresponding daily series 1898–2018, Polar Research, 39,
1037 https://doi.org/10.33265/polar.v39.3614, 2020.

1038 NPI Geological maps: https://geokart.npolar.no/geologi/GeoSvalbard/#6/79.512/19.335, last
1039 access: 12 February 2026.

1040 NPI Map Data and Services: https://geodata.npolar.no/, last access: 10 April 2025.

1041 NPI Svalbardkartet: https://geokart.npolar.no/geologi/GeoSvalbard/#6/79.560/19.355, last
1042 access: 18 February 2026.

1043 Nyall Dawson, Jürgen Fischer, Matthias Kuhn, Alessandro Pasotti, mhugent, Denis Rouzaud,
1044 Alexander Bruy, Tim Sutton, Martin Dobias, Mathieu Pellerin, Even Rouault, Víctor Olaya,
1045 Paul Blottiere, Werner Macho, Radim Blazek, Gary Sherman, Harrissou Sant-anna, Julien
1046 Cabieces, Loïc Bartoletti, Nathan Woodrow, signedav, rldhont, Stefanos Natsis, Larry
1047 Shaffer, Nedjima Belgacem, Sandro Santilli, Salvatore Larosa, Sandro Mani, Jean Felder, and
1048 Vincent Cloarec: qgis/QGIS: 3.44.7, , https://doi.org/10.5281/ZENODO.6139224, 2026.

1049 Orme, L. C., Charman, D. J., Reinhardt, L., Jones, R. T., Mitchell, F. J. G., Stefanini, B. S.,
1050 Barkwith, A., Ellis, M. A., and Grosvenor, M.: Past changes in the North Atlantic storm track
1051 driven by insolation and sea-ice forcing, Geology, 45, 335–338,
1052 https://doi.org/10.1130/G38521.1, 2017.

1053 Paterson, G. A. and Heslop, D.: New methods for unmixing sediment grain size data,
1054 Geochemistry, Geophysics, Geosystems, 16, 4494–4506,
1055 https://doi.org/10.1002/2015GC006070, 2015.

1056 Perkins-Kirkpatrick, S. E. and Lewis, S. C.: Increasing trends in regional heatwaves, Nat
1057 Commun, 11, 3357, https://doi.org/10.1038/s41467-020-16970-7, 2020.

1058 Philippsen, B.: The freshwater reservoir effect in radiocarbon dating, herit sci, 1, 24,
1059 https://doi.org/10.1186/2050-7445-1-24, 2013.

1060 Porter, C., Howat, I., Noh, M.-J., Husby, E., Khuvis, S., Danish, E., Tomko, K., Gardiner, J.,
1061 Negrete, A., Yadav, B., Klassen, J., Kelleher, C., Cloutier, M., Bakker, J., Enos, J., Arnold,
1062 G., Bauer, G., and Morin, P.: ArcticDEM - Mosaics, Version 4.1 (1.0),
1063 https://doi.org/10.7910/DVN/3VDC4W, 2023.

1064 Prins, M. A. and Weltje, G. J.: End-member modeling of siliciclastic grain-size distributions:
1065 The late Quaternary record of aeolian and fluvial sediment supply to the Arabian Sea and its
1066 paleoclimatic significance, in: Numerical experiments in stratigraphy: Recent advances in
1067 stratigraphic and sedimentologic computer simulations, edited by: Harbaugh, J., Society for
1068 Sedimentary Geology, 91–111, 1999.

1069 Rantanen, M., Karpechko, A. Y., Lipponen, A., Nordling, K., Hyvärinen, O., Ruosteenoja, K.,
1070 Vihma, T., and Laaksonen, A.: The Arctic has warmed nearly four times faster than the globe
1071 since 1979, Commun Earth Environ, 3, 1–10, https://doi.org/10.1038/s43247-022-00498-3,
1072 2022.

1073 Rasmussen, C. F., Christiansen, H. H., Buylaert, J.-P., Cunningham, A., Schneider, R.,
1074 Knudsen, M. F., and Stevens, T.: High-resolution OSL dating of loess in Adventdalen,

1075 Svalbard: Late Holocene dust activity and permafrost development, Quaternary Science
1076 Reviews, 310, 108137, https://doi.org/10.1016/j.quascirev.2023.108137, 2023.

1077 Rasmussen, T. L., Forwick, M., and Mackensen, A.: Reconstruction of inflow of Atlantic
1078 Water to Isfjorden, Svalbard during the Holocene: Correlation to climate and seasonality,
1079 Marine Micropaleontology, 94–95, 80–90, https://doi.org/10.1016/j.marmicro.2012.06.008,
1080 2012.

1081 Reimer, P. J., Austin, W. E. N., Bard, E., Bayliss, A., Blackwell, P. G., Ramsey, C. B.,
1082 Butzin, M., Cheng, H., Edwards, R. L., Friedrich, M., Grootes, P. M., Guilderson, T. P.,
1083 Hajdas, I., Heaton, T. J., Hogg, A. G., Hughen, K. A., Kromer, B., Manning, S. W.,
1084 Muscheler, R., Palmer, J. G., Pearson, C., Plicht, J. van der, Reimer, R. W., Richards, D. A.,
1085 Scott, E. M., Southon, J. R., Turney, C. S. M., Wacker, L., Adolphi, F., Büntgen, U., Capano,
1086 M., Fahrni, S. M., Fogtmann-Schulz, A., Friedrich, R., Köhler, P., Kudsk, S., Miyake, F.,
1087 Olsen, J., Reinig, F., Sakamoto, M., Sookdeo, A., and Talamo, S.: The IntCal20 Northern
1088 Hemisphere Radiocarbon Age Calibration Curve (0–55 cal kBP), Radiocarbon, 62, 725–757,
1089 https://doi.org/10.1017/RDC.2020.41, 2020.

1090 Røthe, T. O., Bakke, J., Støren, E. W. N., and Bradley, R. S.: Reconstructing Holocene
1091 Glacier and Climate Fluctuations From Lake Sediments in Vårfluesjøen, Northern
1092 Spitsbergen, Frontiers in Earth Science, 6, 2018.

1093 Rothwell, R. G. and Croudace, I. w.: Twenty Years of XRF Core Scanning Marine
1094 Sediments: What Do Geochemical Proxies Tell Us?, in: Micro-XRF Studies of Sediment
1095 Cores: Applications of a non-destructive tool for the environmental sciences, edited by:
1096 Croudace, I. W. and Rothwell, R. G., Springer Netherlands, Dordrecht, 25–102,
1097 https://doi.org/10.1007/978-94-017-9849-5_2, 2015.

1098 Rymer, K. G., Rachlewicz, G., Buchwal, A., Temme, A. J. A. M., Reimann, T., and Van Der
1099 Meij, W. M.: Contemporary and past aeolian deposition rates in periglacial conditions (Ebba
1100 Valley, central Spitsbergen), CATENA, 211, 105974,
1101 https://doi.org/10.1016/j.catena.2021.105974, 2022.

1102 Salvigsen, O.: Occurrence of pumice on raised beaches and Holocene shoreline displacement
1103 in the inner Isfjorden area, Svalbard, Polar Research, 2, 107–113,
1104 https://doi.org/10.1111/j.1751-8369.1984.tb00488.x, 1984.

1105 Saunders, K. M., Roberts, S. J., Perren, B., Butz, C., Sime, L., Davies, S., Van
1106 Nieuwenhuyze, W., Grosjean, M., and Hodgson, D. A.: Holocene dynamics of the Southern
1107 Hemisphere westerly winds and possible links to CO2 outgassing, Nature Geosci, 11, 650–
1108 655, https://doi.org/10.1038/s41561-018-0186-5, 2018.

1109 Senger, K., Tveranger, J., Ogata, K., Braathen, A., and Planke, S.: Late Mesozoic magmatism
1110 in Svalbard: A review, Earth-Science Reviews, 139, 123–144,
1111 https://doi.org/10.1016/j.earscirev.2014.09.002, 2014.

1112 Simmonds, I. and Rudeva, I.: A comparison of tracking methods for extreme cyclones in the
1113 Arctic basin, Tellus A: Dynamic Meteorology and Oceanography, 66, 25252,
1114 https://doi.org/10.3402/tellusa.v66.25252, 2014.

1115 St. Louis, V. L., St. Pierre, K. A., Emmerton, C. A., Serbu, J. A., Talbot, C. H., Szostek, L.,
1116 Lehnherr, I., Muir, D. C. G., and Criscitiello, A.: Winter Dust Storms Impact the Physical and
1117 Biogeochemical Functioning of a Large High Arctic Lake, Environ. Sci. Technol., 58, 7415–
1118 7424, https://doi.org/10.1021/acs.est.4c00705, 2024.

1119 Stachowska, Z., Van Der Bilt, W. G. M., and Strzelecki, M. C.: Coastal lake sediments from
1120 Arctic Svalbard suggest colder summers are stormier, Nat Commun, 15, 9688,
1121 https://doi.org/10.1038/s41467-024-53875-1, 2024.

1122 Strzelecki, M. C., Lindhorst, S., Hein, C. J., van der Bilt, W. G. M., Kivimaki, K. E., and
1123 Kavan, J.: 10,000 years of centennially-resolved climate and sea-level change archived in
1124 Svalbard beach-ridge system, Sci Rep, https://doi.org/10.1038/s41598-025-33652-w, 2026.

1125 Tanaka, H. L., Yamagami, A., and Takahashi, S.: The structure and behavior of the arctic
1126 cyclone in summer analyzed by the JRA-25/JCDAS data, Polar Science, 6, 55–69,
1127 https://doi.org/10.1016/j.polar.2012.03.001, 2012.

1128 Thió-Henestrosa, S. and Comas, M.: CoDaPack 2.0: a stand-alone, multi-platform
1129 compositional software, Proceedings of CoDaWork'11: 4th international workshop on
1130 Compositional Data Analysis, Egozcue, J.J., Tolosana-Delgado, R. and Ortego, M.I. (eds.)
1131 2011, Accepted: 2022-05-03T15:17:28Z, 2011.

1132 Toonen, W. H. J., Winkels, T. G., Cohen, K. M., Prins, M. A., and Middelkoop, H.: Lower
1133 Rhine historical flood magnitudes of the last 450years reproduced from grain-size
1134 measurements of flood deposits using End Member Modelling, CATENA, 130, 69–81,
1135 https://doi.org/10.1016/j.catena.2014.12.004, 2015.

1136 Vos, K., Vandenberghe, N., and Elsen, J.: Surface textural analysis of quartz grains by
1137 scanning electron microscopy (SEM): From sample preparation to environmental
1138 interpretation, Earth-Science Reviews, 128, 93–104,
1139 https://doi.org/10.1016/j.earscirev.2013.10.013, 2014.

Zolitschka, B., Francus, P., Ojala, A. E. K., and Schimmelmann, A.: Varves in lake sediments – a review, Quaternary Science Reviews, 117, 1–41, https://doi.org/10.1016/j.quascirev.2015.03.019, 2015.

Tables with captions

Lab code	Depth (cm)	Material	Dry weight (mg)	^{14}C age (yrs B.P.)	Error (^{14}C yrs)	Cal. yrs B.P.
Poz-173765	16.25	*Aquatic moss*	17	-602	25	-52 to -55
Poz-173976	16.25	*Terrestrial plants*	1.7	1,265	30	1,283 to 1,176
Poz-173973	53.75	*Aquatic moss*	5.3	4,010	30	4,529 to 4,415
Ua-85772	94	*Terrestrial plants*	1.6	6,352	49	7,339 to 7,165
Poz-173975	95	*Aquatic moss*	1.3	1,575	30	1,526 to 1,391
Poz-173974	117	*Aquatic moss*	12.3	-123	24	-66 to -69
Poz-173977	117	*Terrestrial plants*	1.1	7,150	40	8,020 to 7,930

Table 1. Radiocarbon sample overview. All dating samples were extracted from the analysed DST-2023 GC core. Calibrated ages, errors, and ranges (2σ) are based on the Intcal20 curve (Reimer et al., 2020), and the calibration was performed using the Bayesian Bacon R package v.3.3.1 (Blaauw et al., 2022). Gray text marks outliers.

	CT	clr Ca	clr Ti	clr Fe	DBD	LOI	MGS	log EM 1	log EM 2
clr Ca	-0.33								
clr Ti	0.54	-0.94							
clr Fe	0.30	-0.95	0.89						
DBD	0.68	*0.14*	*0.05*	*-0.18*					
LOI	-0.67	*-0.13*	*-0.07*	*0.15*	-0.89				
MGS	0.38	-0.42	0.49	0.44	0.22	-0.22			
log EM 1	-0.49	0.21	-0.31	-0.24	-0.40	0.46	-0.83		
log EM 2	0.29	0.22	*-0.03*	*-0.15*	0.52	-0.61	*0.16*	-0.57	
log EM 3	*-0.01*	-0.42	0.33	0.40	*-0.18*	0.26	0.66	-0.27	-0.53

Table 2. Proxy correlations. Black values reflect Spearman's correlation coefficients (ρ), while gray values show cross-correlation between physical analyses and the resampled scanning data (r). Values shown in italics reflect results with p>0.05.

Figures with captions

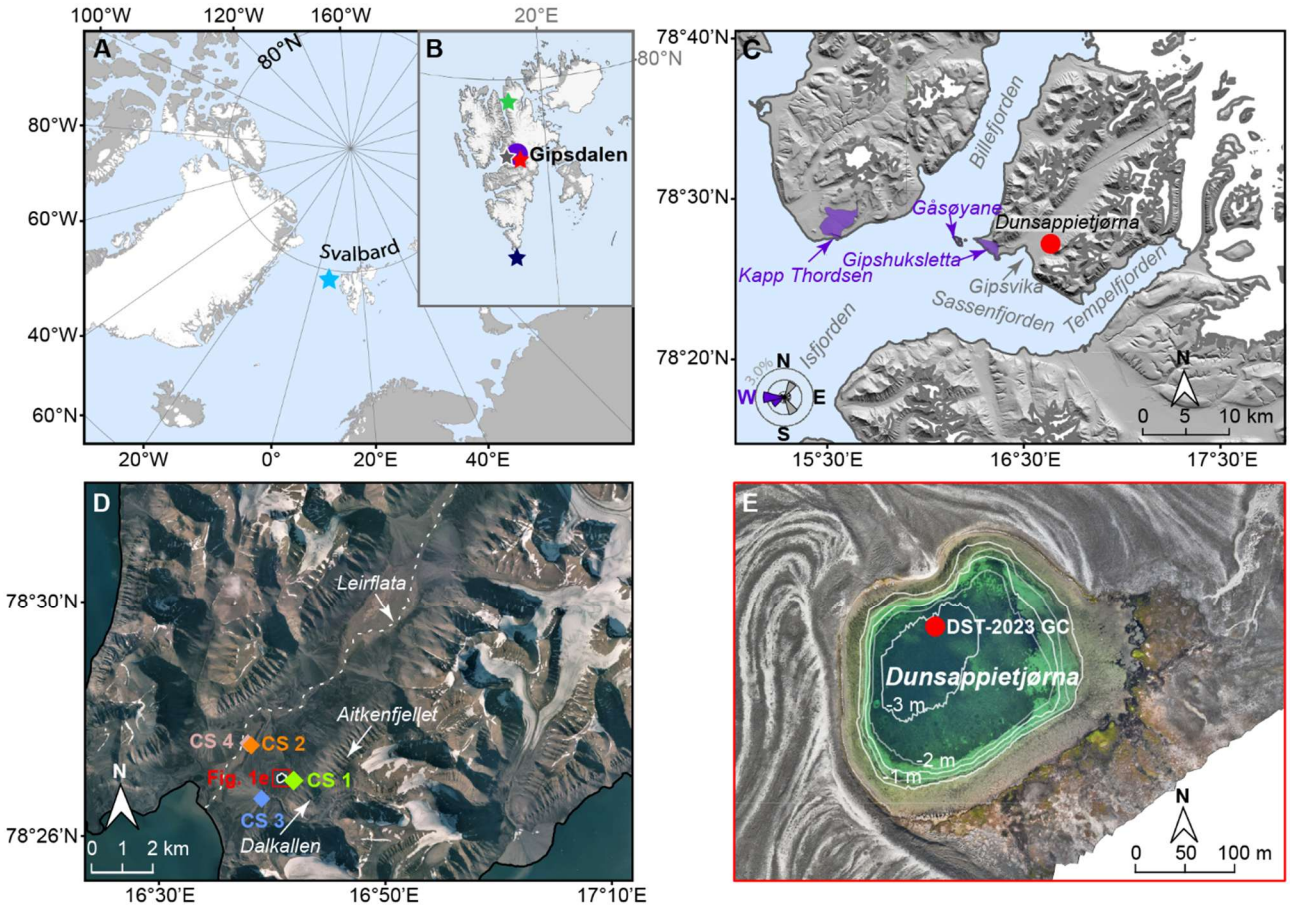

Figure 1. Study area and site location. A. Location of the Svalbard archipelago in a North Atlantic-Arctic climate context. The light blue star marks the location of the P_BIP_{25}-derived sea-ice coverage data in Eastern Fram Strait (Müller et al., 2012a, b). **B.** Close-up of Svalbard, showing the location of Gipsdalen (purple dot), Westerly wind reconstruction from Steinbruvatnet (dark blue star; Stachowska et al., 2024); temperature anomalies from Fiskedammane 3 – a closed lake in Northern Spitsbergen (green star; Kong et al., 2025), relative

sea-level (RSL) curve from Bjonasletta beach-ridge plain in Central Spitsbergen (red star; Strzelecki et al., 2026), ice-rafted debris (IRD) data from core JM98-845-PC collected in Central Isfjorden (gray star with white outline; Rasmussen et al., 2012). **C.** ArcticDEM-derived topography illustrating valley-fjord meridional orientation (Porter et al., 2023), major fjords (gray labels), glaciers and ice caps (white), and key locations: the study site (red dot), as well as dolerite outcrops in Gipshuksletta, Gåsøyane, and Kapp Thordsen (outlined in purple; GeoSvalbard: NPI Geological maps, 2026; Brekke and Hansson, 1990; Nejbert et al., 2011; Senger et al., 2014). The wind rose represents July-September wind direction data from the Gåsøyane lighthouse station (2023-2024; Frank et al., 2023b). **D.** Satellite imagery of the Dunsappietjørna catchment (NPI Map Data and Services, 2025), showing the locations of catchment samples (CSs 1-4), Leirflata floodplain, two mountains – Dalkallen and Aitkenfjellet, and Gipsdalselva (white dashed line). **E.** Drone imagery of Dunsappietjørna with bathymetry presented with 0.5 m contour isobaths (white lines). The location of the studied sediment core DST-2023 GC is highlighted in red.

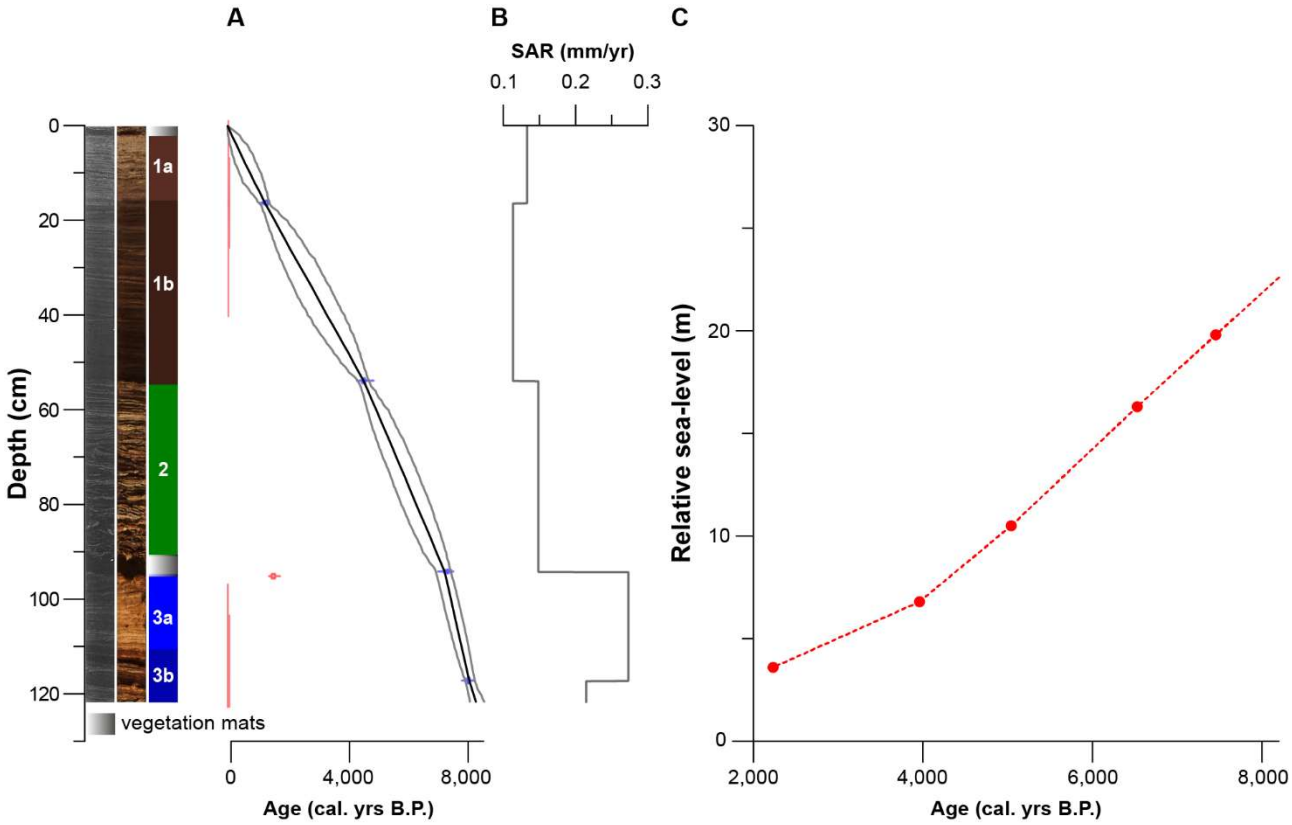

1179

1180 **Figure 2. Chronology and sedimentation.** From the left: CT and optical imagery, and units-
1181 subunits classification of the sedimentary record (see 'The Mid- and Late Holocene evolution
1182 of Dunsappietjørna'). **A.** Our age-depth model: the black line represents the weighted mean
1183 best fit, while the gray lines depict the 95% confidence interval. Calibrated ^{14}C age distributions
1184 are marked in blue (included), while red indicates anomalously young ages (outliers). **B.**
1185 Sediment Accumulation Rate values (SAR; in mm/yr). **C.** Local RSL curve from Bjonasletta
1186 beach-ridge plain in Central Spitsbergen (see also Fig. 1B; Strzelecki et al., 2026). We only
1187 present the available timing coeval with our record.

1188

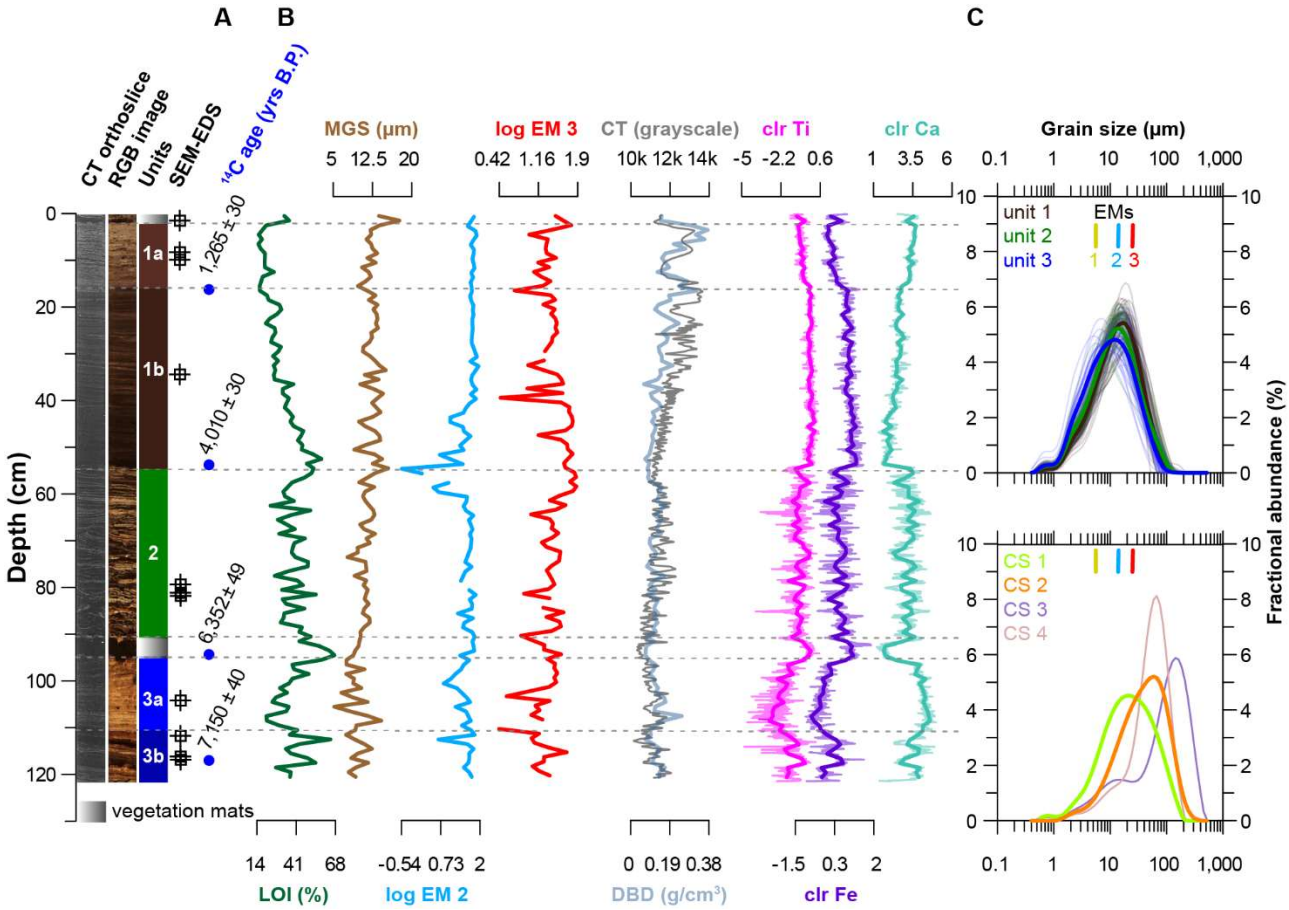

Figure 3. Key proxies and grain-size statistics measured on Dunsappietjørna sediments. From the left: CT and optical imagery, and unit-subunit classification of the sedimentary record. **A.** Position of samples selected for Scanning Electron Microscopy (SEM) imagery and Energy Dispersive X-ray Spectroscopy (SEM-EDS; left), and position of ^{14}C samples with ^{14}C ages ± errors (yrs; right). **B.** Organic content – shown by Loss on Ignition (LOI, %; Dean, 1974; Heiri et al., 2001), the grain-size variability – reflected by mean grain-size (MGS) values in µm, and logarithmic (log) ratios for the grain-size End Member Modelling (EMMA) output, reflected by End Members (EMs) 2 and 3 (Dietze et al., 2022; Prins and Weltje, 1999), density – captured by CT grayscale values shown on top (Cnudde and Boone, 2013), and Dry Bulk Density (DBD) shown on the bottom, minerogenic input – reflected by centred log-ratios (clr) of titanium (Ti; Auer et al., 2025; Stachowska et al., 2024), and iron (Fe; Bertrand et al., 2024; Davies et al., 2015), carbonate deposition – measured by clr calcium (Ca; Davies et al., 2015). **C.** The grain-size distributions of samples from each unit (*n*=121), and colour-coded accordingly, with the

unit mean curves highlighted in bold and the grain-size means of three EMs marked above (top); CSs 1-4 (bottom; see also Figs. 1D and S1) – presented on a μm scale.

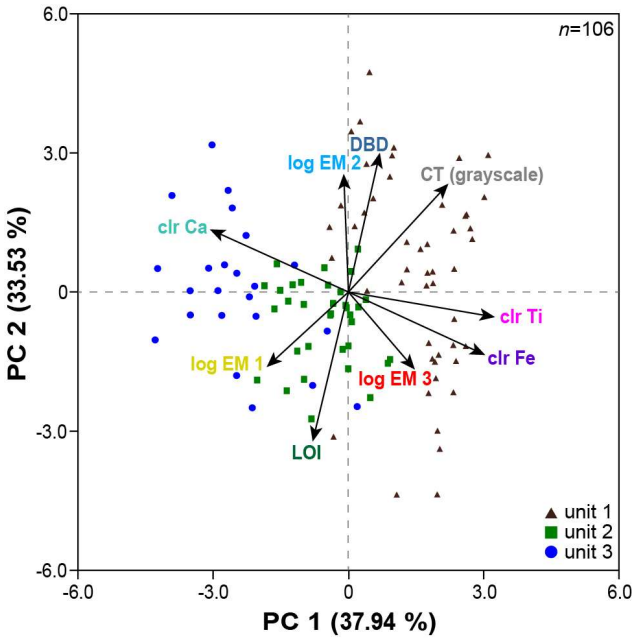

Figure 4. Ordination diagram. The vectors (arrows) represent the confidence scores of selected variables on principal components (PCs) 1 and 2, which together account for most of the explanatory power. Samples were colour-coded according to the unit classification shown in Figs. 2-3, while proxies were colour-coded as in Fig. 3B-C. Factor loadings for PCs 1 and 2 are presented in Table S1.

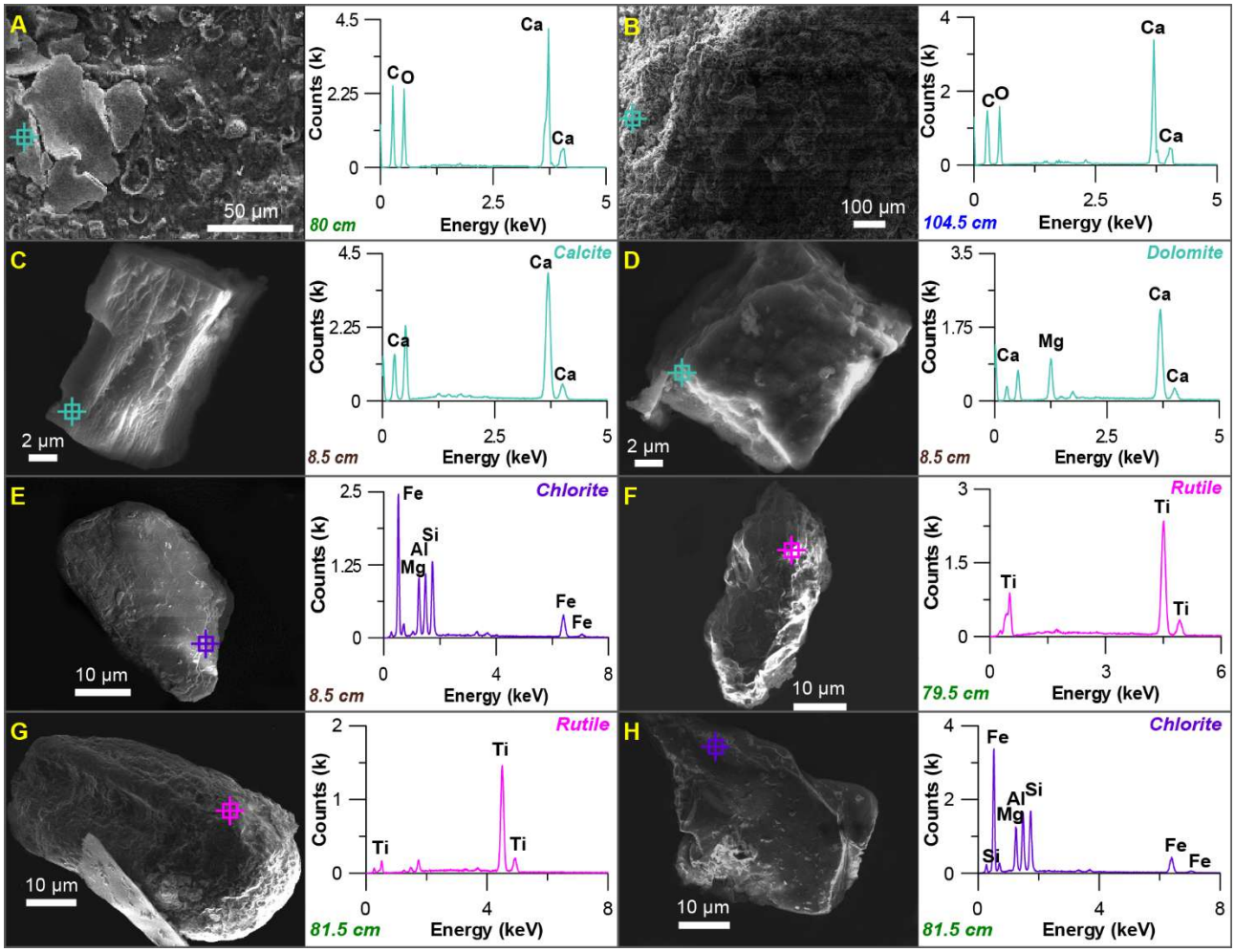

Figure 5. SEM images and SEM-EDS spectra of authigenic carbonates, and representative clastic carbonate and Fe-Ti-rich material. A-B. Authigenic Ca carbonates from subunits 2a and 3a (80 and 104.5 cm, respectively). **C-D.** Detrital <20 µm carbonate clasts (calcite and dolomite) from subunit 1a (8.5 cm) within the EM 2 modal range. **E-H.** Detrital >20 µm Fe-Ti-rich clasts (presumably chlorite and rutile) from subunit 1a (8.5 cm) and unit 2 (79.5 and 81.5 cm) within EM 3 modal grain-size range. Crosshairs indicate EDS analysis spots, while adjacent spectra correspond to the marked locations. SEM-EDS elemental or oxide compositions and the interpreted mineralogy are listed in Tables S2-S3. Colour-coding follows the proxy colouring presented in Figs. 3B and 4.

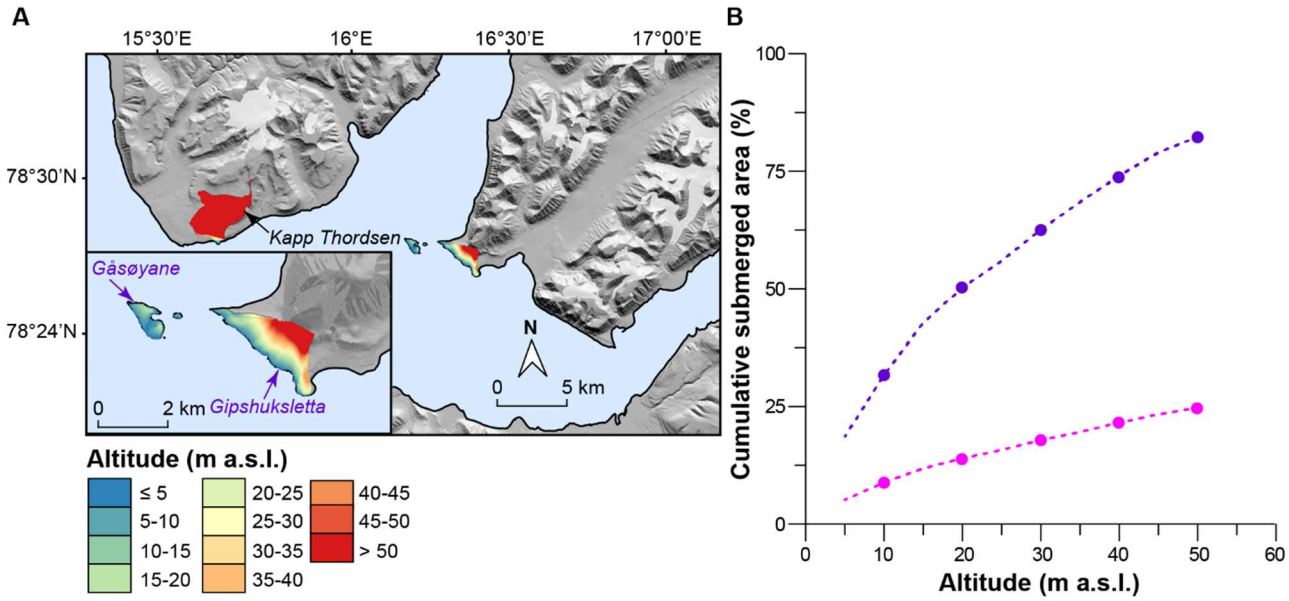

1223

1224 **Figure 6. ArcticDEM 2 m mosaic-derived altitude and cumulative hypsometry of mapped**
1225 **dolerite outcrop areas** (NPI Geological maps, 2026; Porter et al., 2023)**. A.** Map of the studied
1226 dolerite outcrops in Kapp Thordsen, Gåsøyane and Gipshuksletta, coloured by altitude classes
1227 (m a.s.l.; Porter et al., 2023). **B.** Cumulative submerged area expressed as % of dolerite outcrop
1228 area at or below a given altitude. The curves show the % of area that would be submerged if
1229 RSL reached that altitude (see also Fig. 2C), with the purple curve showing Gåsøyane and
1230 Gipshuksletta, and the magenta curve showing the combined area including Kapp Thordsen
1231 (see also Table S5; Porter et al., 2023).

1232

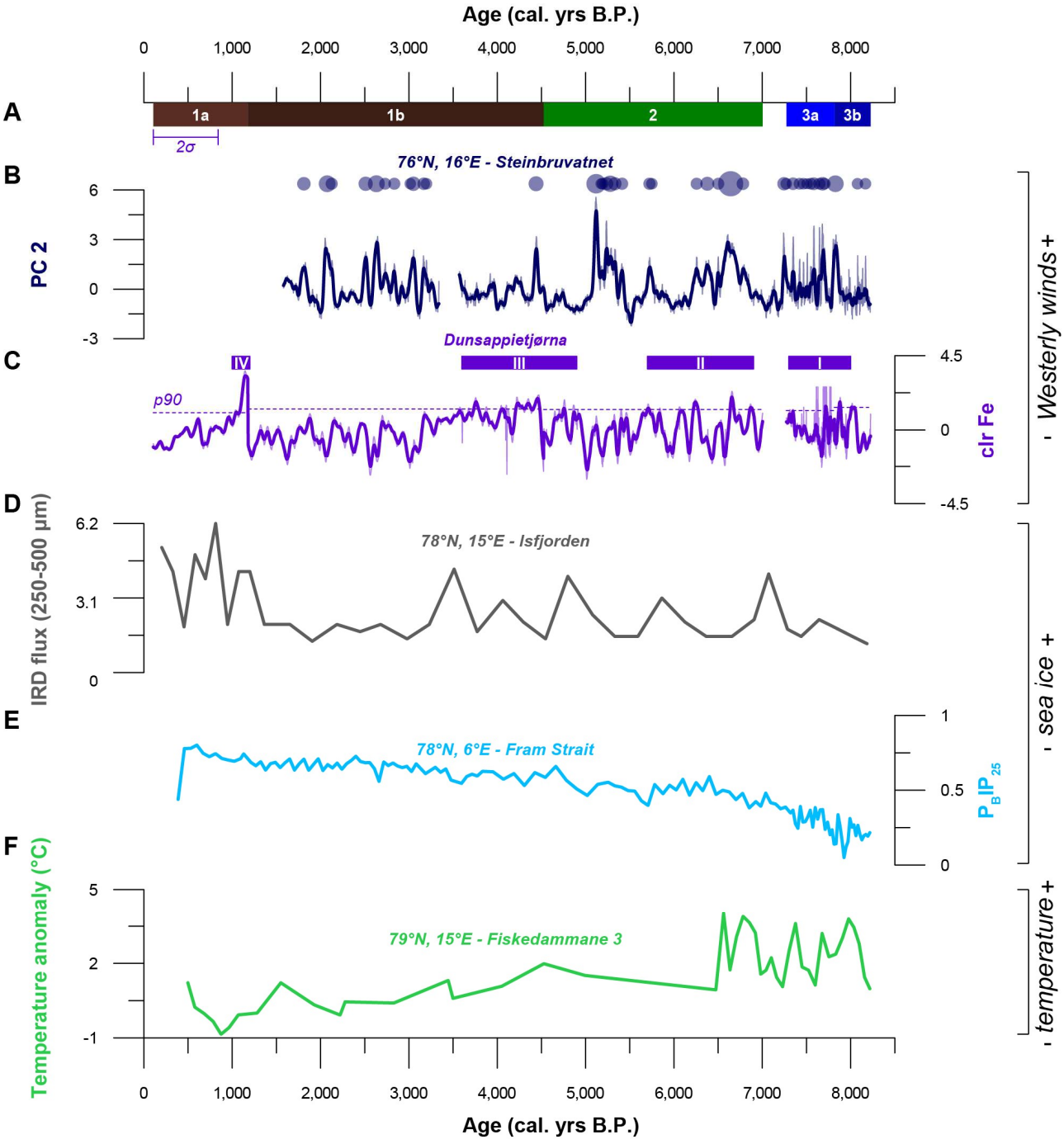

Figure 7. Comparison of our clr Fe-derived Mid- and Late Holocene Westerly wind reconstruction from Dunsappietjørna with relevant paleorecords from Svalbard and Fram Strait. Colour coding matches that presented in Fig. 1A-B, where we also map site locations. **A.** Lithostratigraphic unit-subunit classification of the Dunsappietjørna record. The purple horizontal bar marks the average calibrated 2σ age uncertainty of the record based on the age-depth model presented in Fig. 2a. **B.** PC 2-based Westerly wind reconstruction from

Steinbruvatnet, Southern Svalbard, with 30-year averages in bold and PC-2 derived Storm Magnitude Index (SMI) values calculated for maxima in Westerly winds, and shown as scaled circles (Stachowska et al., 2024). **C.** Clr Fe-based Westerly wind reconstruction from Dunsappietjørna, Central Spitsbergen, Svalbard (purple), standardised per units or subunits (Toonen et al., 2015), with 30-year averages in bold. Wind maxima are identified using a 90th percentile (*p90*) threshold (Hobday et al., 2016; Perkins-Kirkpatrick and Lewis, 2020), applied within each unit or subunit (see Fig. S8 for more details). Four major phases of the Mid- and Late Holocene Westerly maxima are marked by purple rectangles above the clr Fe curve and labelled with white Roman numerals. **D.** Central Isfjorden ice-rafted debris (IRD) record, plotted as IRD flux in the 250-500 μm size fraction from core JM98-845-PC (Rasmussen et al., 2012). **E.** Sea-ice cover data from Fram Strait (light blue), based on P_BIP_{25} (Müller et al., 2012a, b). **F.** Spring temperature reconstruction from the closed Fiskedammane 3 – a lake in Northern Spitsbergen (green), based on U_{37}^{K} (Kong et al., 2025).

Supplementary Information

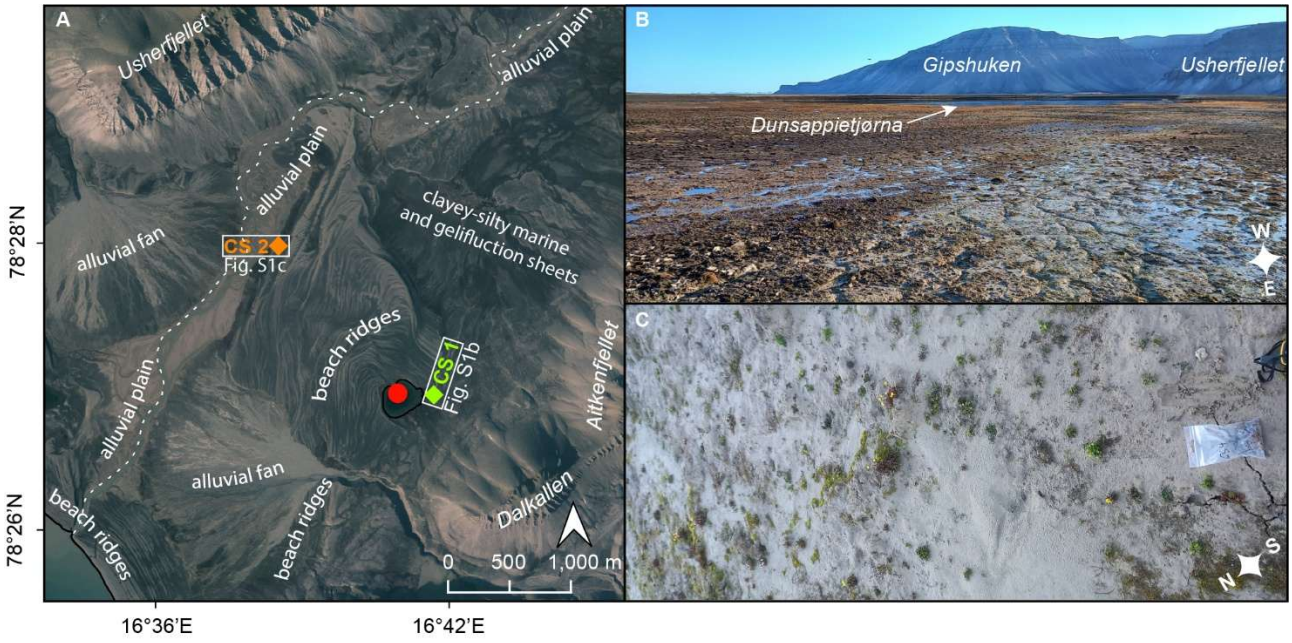

Figure S1. Catchment geomorphology and sedimentology of the Southern Gipsdalen. A. Aerial imagery of the study area, highlighting key geomorphic and sedimentary features (NPI Map Data and Services, 2025). The locations of the studied sediment core DST-2023 GC (red dot), the river – Gipsdalselva (dashed white line), and catchment samples (CSs) 1-2 (green and light blue, respectively). **B**. Field photograph from the CS 1 location, showing ephemeral streams flowing through the clayey-silty ground, Northeast of Dunsappietjørna. The lake basin, Gipshuken and Usherfjellet are visible in the background. **C.** Field photograph from the CS 2 location, showing sedimentary deposits and tundra vegetation in the alluvial plain of the Gipsdalselva, Northwest of the lake.

Figure S2. Sentinel-2 satellite imagery (July 2023) showing peak dust accumulation in the area (ESA, EC, 2023)**.** The study site is marked with a red dot.

Supplementary Note 1: Wind data from the Gåsøyane lighthouse station (2023-2024)

Winter (DJF) is characterised by valley-induced North and Northeasterly winds, which prevail 29% of the time with an average speed of 9.9 m/s (fresh breeze). While significant, the Easterlies are weaker, occurring 22% of the time at an average speed of 8.5 m/s (approximately a fresh breeze). Westerly winds are rare but occasionally the strongest, accounting for 8% of winter observations, with a mean speed of 12.3 m/s (strong breeze). On the contrary, Westerlies dominate in the summer (JJA), prevailing 45% of the time, though they are weaker, averaging 5.3 m/s (gentle breeze). Winds descending from the valley's North maintain their strength and influence, occurring 21% of the time at an average speed of 7.0 m/s (moderate breeze), making them the most powerful summer system. Additionally, Southeasterlies occur 23% of the time at 5.8 m/s (moderate breeze; Frank et al., 2023).

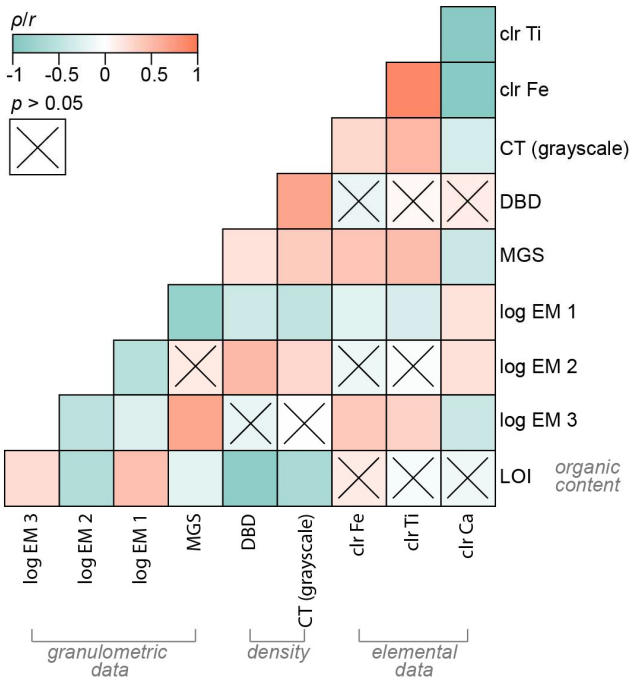

Figure S3. Proxy correlations. We calculated Spearman's rank correlation coefficients (ρ) for all proxy pairs, except for comparisons between physical measurements and resampled scanning data, for which we applied cross-correlation (r; see 'Methods' and Table 2 in the main manuscript). Crossed-out boxes indicate results with p>0.05. The graph was prepared in ChiPlot (ChiPlot, 2023).

Supplementary Note 2: Authigenic carbonates in Dunsappietjørna sediments

In-lake carbonate precipitation typically occurs during whiting events, most pronounced in summer, when rising water temperatures reduce calcite solubility, thereby promoting precipitation. The extent of this process is influenced by multiple factors, including seasonal hydrology, water pH and hardness, phytoplankton blooms, and primary productivity (Boyall et al., 2023; Küchler-Krischun and Kleiner, 1990; Mazurek et al., 2012; Ohlendorf and Sturm, 2001; Vanderploeg et al., 1987). Unlike in spring, when medium- to coarse-grained calcite precipitates, summer precipitation is dominated by smaller endogenic particles because the

formation of larger crystals is primarily driven by longer growth durations (Boyall et al., 2023; Küchler-Krischun and Kleiner, 1990).

The presence of flake-like, anhedral authigenic carbonates (~10-50 µm; see Fig. 5A-B in the main manuscript) suggests that carbonate is preserved in a partially different form, compared to the intact crystals or other forms described in (Boyall et al., 2023; Küchler-Krischun and Kleiner, 1990; Mazurek et al., 2012; Vanderploeg et al., 1987). However, unlike in other hardwater cold lake studies by Ohlendorf and Sturm (2001), where prolonged exposure to undersaturated bottom waters during the ice-cover season results in complete calcite dissolution, conditions in Dunsappietjørna favour partial preservation. Although we lack sediment-trap data and direct observations, the conservation of authigenic carbonates is likely due to high precipitation rates, as shown by sections with the highest authigenic carbonate content, which coincide with peak sediment accumulation rates (SARs; see also Fig. 2B in the main manuscript). In lakes with high calcite fluxes (>60% sediment calcite content), rapid burial prevents calcite from dissolving (Lotter et al., 1997).

Additionally, we want to emphasise that the possibility of biologically induced calcite precipitation cannot be ruled out, as the ice-free period coincides with peak lake temperatures and potential phytoplankton blooms. Algal activity can promote the formation of ~30 µm calcite crystals at water temperatures as low as +4°C, likely due to photosynthetic CO_2 uptake by plankton in late summer (Ohlendorf and Sturm, 2001). During March 2024 fieldwork, we observed a dense algal mat on the sediment surface, likely a remnant of the last bloom (see also the ‘4.1. Core chronology’ in the main manuscript).

Variable	PC 1	PC 2
DBD	0.11	0.47
LOI	-0.12	-0.51
log EM 1	-0.28	-0.25
log EM 2	-0.02	0.40
log EM 3	0.23	-0.26
CT (grayscale)	0.35	0.37
clr Ca	-0.48	0.21
clr Ti	0.51	-0.08
clr Fe	0.48	-0.21

71 **Table S1. Principal Component Analysis factor loadings.** Data shown for the two most
72 significant (71.47%) Principal Components (PCs) 1 and 2. For more details, see our 'Methods',
73 as well as 'Results and Discussion' sections in the main manuscript.

74

Fig. 5 panel	Depth (cm)	C	O	Mg	Al	Si	S	Ca
A	80	10.64	45.16	0.00	0.00	0.26	0.00	43.66
B	104.5	9.99	42.13	0.29	0.34	0.54	0.61	46.09

75 **Table S2. SEM-EDS elemental compositions (wt%) of authigenic carbonates.** Each entry
76 corresponds to an SEM-EDS spectrum shown in Fig. 5A-B (see the main manuscript).

77

Figure and panel	Depth (cm) or source	Na_2O	MgO	Al_2O_3	SiO_2	P_2O_5	K_2O	CaO	TiO_2	MnO	Fe_2O_3	Interpreted mineralogy
5C	8.5	0.10	1.23	0.85	1.32	0.00	0.00	95.40	0.47	0.24	0.35	calcite
5D	8.5	0.22	28.96	3.51	6.87	0.21	0.24	58.67	0.00	0.07	1.13	dolomite
5E	8.5	1.65	15.16	16.84	26.29	0.08	1.09	1.21	0.13	0.63	36.94	chlorite
5F	81.5	0.00	0.28	0.38	1.17	0.00	0.01	0.22	97.23	0.00	0.71	rutile
5G	81.5	0.00	0.50	1.24	3.59	0.03	0.42	0.95	92.93	0.00	0.33	rutile
5H	81.5	0.26	14.78	21.20	28.31	0.00	0.57	1.15	0.16	0.28	33.28	chlorite
S6A	CS 1	0.22	11.16	1.61	4.70	0.00	0.27	79.62	0.16	0.15	1.91	dolomite
S6B	CS 1	0.36	15.17	1.03	3.10	0.00	0.20	79.02	0.26	0.00	0.29	dolomite

Table S3. SEM-EDS oxide compositions (wt%) of detrital carbonate grains and Fe-Ti-rich, dolerite-derived clasts, together with interpreted mineral phases. Oxide data were normalised to 100 wt% prior to mineral identification. Each row reports a representative spectrum for the grains shown in Figs. 5C-H and S6A-B, as multiple spectra (typically n=5 or 6) were acquired per grain to assess its oxide composition.

Depth (cm) or source	Na_2O	MgO	Al_2O_3	SiO_2	P_2O_5	K_2O	CaO	TiO_2	MnO	Fe_2O_3	Interpreted mineralogy
79.5	1.03	15.92	24.92	33.25	0.22	1.82	0.46	0.22	0.00	22.16	Fe-rich mica or chlorite
79.5	1.00	8.38	18.75	48.74	0.79	4.75	9.40	0.03	0.10	8.05	hornblende or Ca-rich plagioclase
81.5	1.98	14.56	24.70	50.33	0.31	2.04	4.17	1.77	0.00	0.13	altered chlorite
81.5	0.28	6.62	16.98	37.58	0.13	8.57	0.83	3.41	0.95	24.64	biotite
CS 2	0.82	13.18	19.28	43.31	0.19	3.79	1.11	0.30	0.08	17.94	biotite
CS 2	1.00	15.21	14.80	38.57	0.41	3.43	6.53	0.37	0.13	19.55	biotite

Table S4. Additional SEM-EDS oxide compositions (wt%) of Fe-Ti-rich, dolerite-derived clasts, together with interpreted mineral phases, provided for completeness and not illustrated in Fig. 5. Oxide data were normalised to 100 wt% prior to mineral identification. Each row reports a representative spectrum, as multiple spectra (typically n=5 or 6) were acquired per grain to assess its oxide composition.

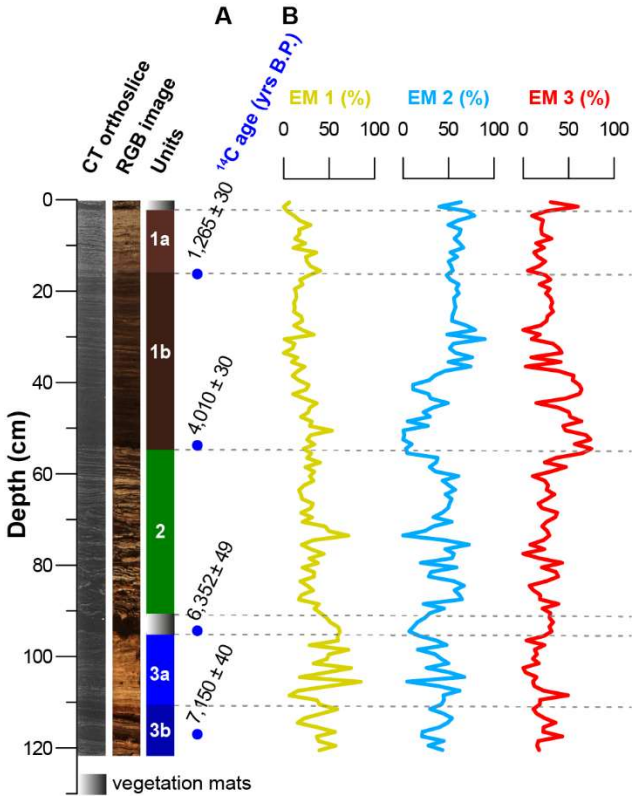

Figure S4. End-Member Modelling Analysis (EMMA) results (Dietze et al., 2022; Prins and Weltje, 1999). From the left: CT and optical imagery, and (sub)units classification of the sedimentary record. **A.** Position of ^{14}C samples with ^{14}C ages ± errors (yrs). **B.** Downcore variability in EMs abundances (%; Prins and Weltje, 1999). Colour-coding for EMs follows the proxy colouring shown in Figs. 3B-C and 4 of the main manuscript.

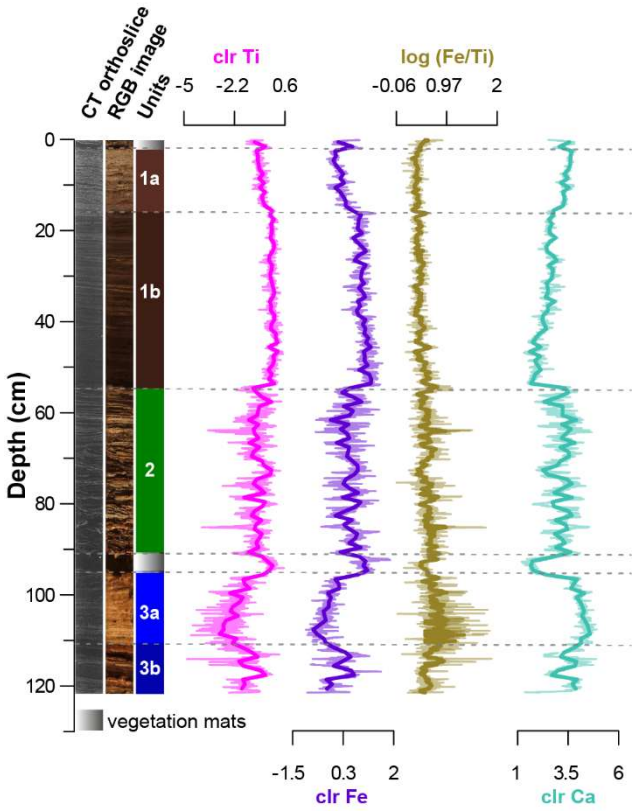

94

95 **Figure S5. Key proxies for detrital input and variations in the non-detrital Fe measured**
96 **in Dunsappietjørna sediments.** From the left: CT orthoslice and RGB image with
97 lithostratigraphic units; centred log-ratios (clr) of Ti and Fe as proxies for minerogenic input
98 (Auer et al., 2025; Bertrand et al., 2024; Davies et al., 2015; Stachowska et al., 2024); log(Fe/Ti)
99 ratio, isolating the non-detrital Fe component (Blanchet et al., 2009; Davies et al., 2015); and
100 clr calcium (Ca) as a proxy for carbonates (Davies et al., 2015). Elevated log(Fe/Ti) values
101 indicate intervals where Fe variability is likely influenced by processes other than clastic input,
102 e.g., redox-related processes (Blanchet et al., 2009; Davies et al., 2015; Kylander et al., 2011),
103 while negative or stable values suggest dominance of detrital Fe co-varying with Ti (see also
104 'The Mid- to Late Holocene evolution of Dunsappietjørna' in the main manuscript). Colour-
105 coding for clr Ti, Fe and Ca follows the proxy colouring shown in Figs. 3B, 4 and 5 of the main
106 manuscript.

107

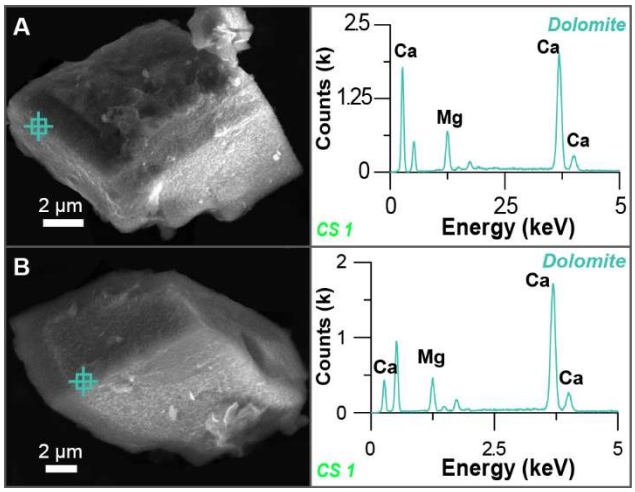

Figure S6. SEM images and SEM-EDS spectra of carbonate clasts identified in CS 1 (A-B). Crosshairs indicate EDS analysis spots, while adjacent spectra correspond to the marked locations. SEM-EDS elemental compositions and the interpreted mineralogy are listed in Table S3. Colour-coding follows the proxy colouring presented in Figs. 3B and 4 of the main manuscript.

Altitude (m a.s.l.)	G-G area (m^2)	G-G-K. T. area (m^2)	G-G total %	G-G-K. T. total %	G-G cumulative %	G-G-K. T. cumulative %
0-5	650735	691274	18.59	5.17	18.59	5.17
5-10	458720	487525	13.1	3.65	31.69	8.82
10-15	389376	405382	11.12	3.03	42.81	11.85
15-20	260296	280568	7.43	2.1	50.24	13.95
20-25	200563	244306	5.73	1.83	55.97	15.78
25-30	231492	270969	6.61	2.03	62.58	17.81
30-35	205885	240029	5.88	1.8	68.46	19.6
35-40	194158	261379	5.55	1.96	74.01	21.56
40-45	174951	237904	5	1.78	79.01	23.34
45-50	114152	177105	3.26	1.33	82.27	24.66

Table S5. Hypsometric area distribution of mapped dolerite outcrops derived from the 2 m ArcticDEM mosaic (Porter et al., 2023). Outcrop area (m^2) is reported for 5 m altitude bins (m a.s.l.) for two spatial extents: G-G (Gåsøyane and Gipshuksletta) and G-G-K. T. (Gåsøyane and Gipshuksletta combined with Kapp Thordsen; see Fig. 6A-B in the main manuscript). 'Total %' shows the proportion of the total outcrop area falling within each altitude bin, while 'cumulative %' gives the proportion of outcrop area lying at or below each altitude bin upper limit, corresponding to the fraction that would be submerged if relative sea-level (RSL) reached that altitude (see also Fig. 2C in the main manuscript).

Supplementary Note 3: Mid- and Late Holocene evolution of dolerite source availability under relative sea-level change and implications for signal stability

The gradual stabilisation of the Fe-Ti-rich dolerite-derived signal throughout the DST-2023-GC record is unlikely to reflect wind variability alone, but also changes in source-area availability linked to glacio-isostatic uplift and relative sea-level (RSL) fall, as discussed in section 4.3 and illustrated in Figs. 3C and 6A-B of the main manuscript. Importantly, we do not geochemically fingerprint the dolerite-derived fraction to a specific outcrop, and therefore treat the mapped outcrops as a combined set of source areas.

Within that framework, the local RSL curve (Fig. 2C) implies that at the onset of the DST-2023-GC record (Strzelecki et al., 2026), a substantial % of the nearest, low-lying dolerite outcrop area on Gåsøyane and Gipshuksletta would have been submerged (purple curve in Fig. 6B), reducing the subaerial area available for deflation and entrainment of dolerite-derived material. This might help to contextualise the comparatively weaker Fe-Ti-rich input in unit 3 compared to the rest of the record (see 4.2.2 of the main manuscript), even under favourable Westerly winds. As emergence progressed through the Mid- and Late Holocene, the % of submerged outcrop area dropped, favouring more persistent dolerite-derived input. When the higher-altitude Kapp Thordsen outcrops are included (Fig. 6A and magenta curve in 6B), the cumulative submerged area remains much lower across the same altitude range, indicating that a broader, mixed source domain would have been less sensitive to early RSL.

We also note that if low-lying outcrops dominated the dolerite signal, it should be most sensitive to RSL-driven exposure changes. In contrast, a substantial contribution from higher-altitude

outcrops would likely dampen that sensitivity. These hypsometry-based constraints therefore support interpreting the Mid- and Late Holocene signal enhancement as partly a source-availability effect, without addressing site-specific provenance.

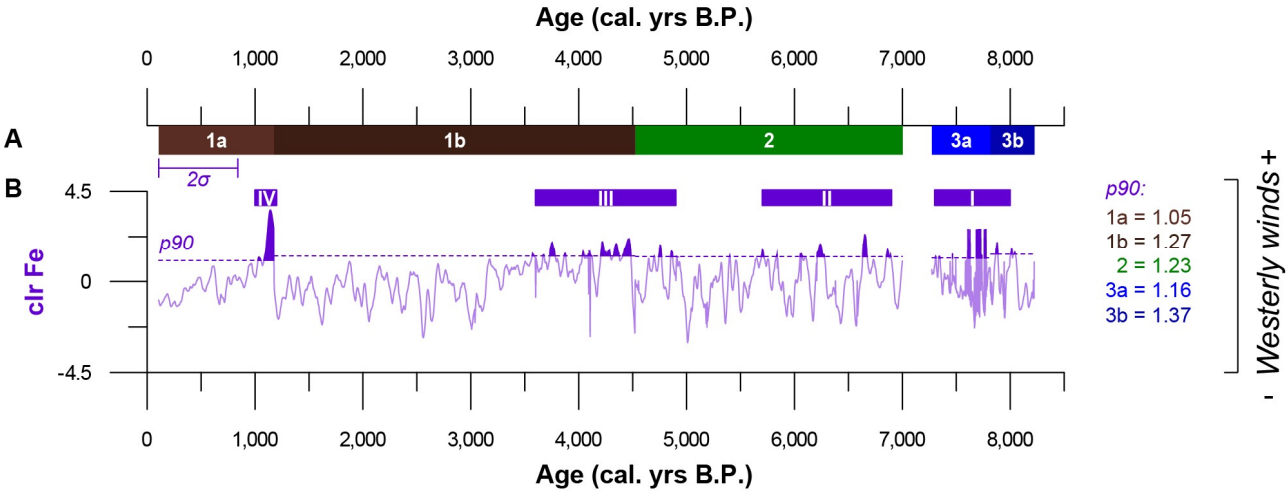

Figure S7. Clr Fe-derived Mid- and Late Holocene Westerly wind reconstruction from Dunsappietjørna sediments, Central Spitsbergen, Svalbard. A. Lithostratigraphic unit-subunit classification of the record. The purple horizontal bar indicates the average calibrated 2σ age uncertainty for the record, based on the age-depth model shown in Fig. 2A of the main manuscript. **B.** Clr Fe-based Westerly wind reconstruction from the record, standardised per units or subunits (Toonen et al., 2015), with 30-year averages in bold. Wind maxima are identified using a 90th percentile (*p90*) threshold (Hobday et al., 2016; Perkins-Kirkpatrick and Lewis, 2020), applied within each unit or subunit. Four major phases of the Mid- and Late Holocene Westerly maxima are marked by purple rectangles above the clr Fe curve and labelled with white Roman numerals. Colour-coding for clr Fe follows the proxy colouring shown in Figs. 3B, 4, 5E, H and 7C of the main manuscript.

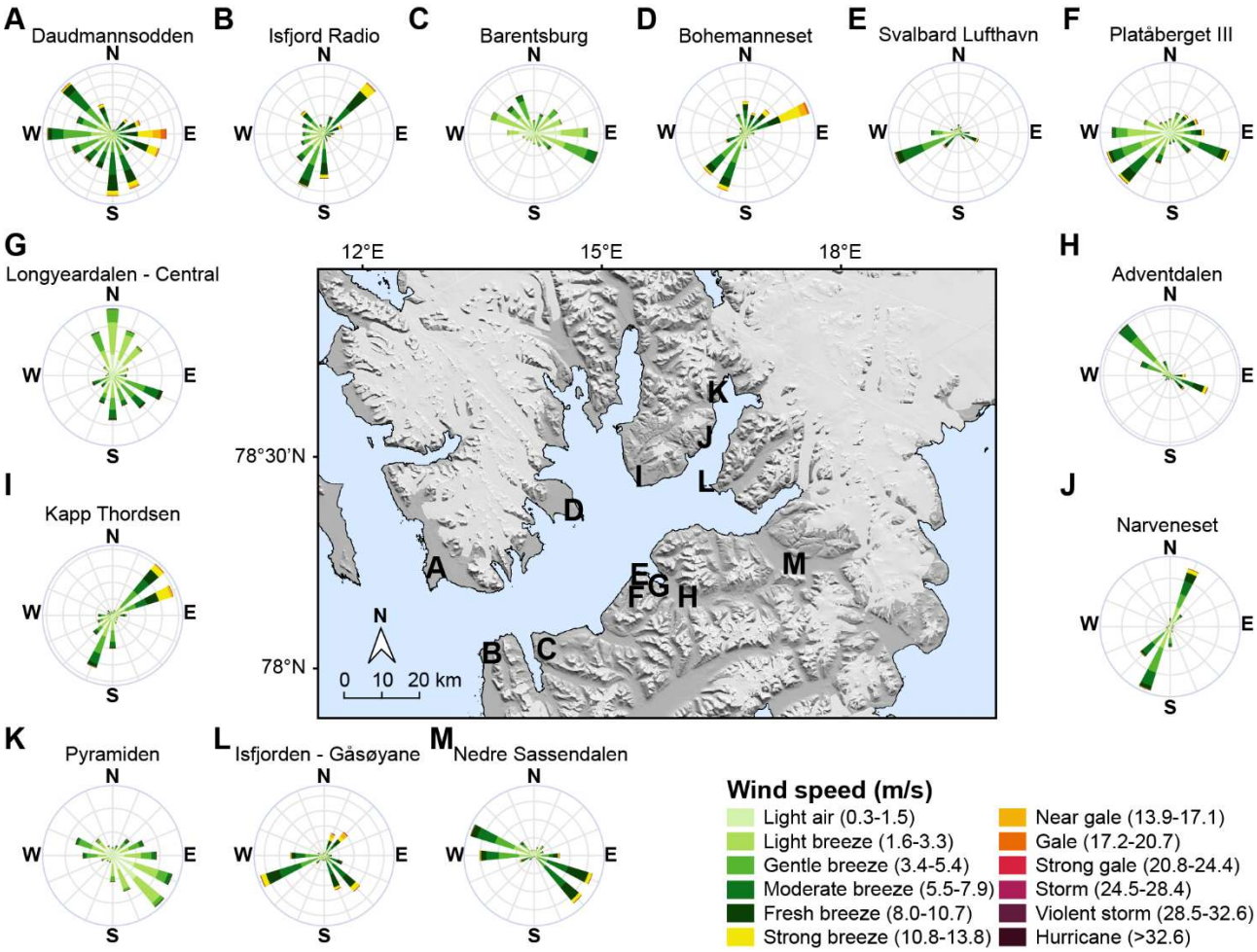

Figure S8. June-August (JJA) wind roses and wind speed data (m/s) from 13 weather stations located in Isfjorden (in the centre). Data for recurring JJA periods between 2015 and 2025 (MET Norway, 2026). **A.** Daudmannsodden (2025). **B.** Isfjord Radio (2015-2025). **C.** Barenstburg (2015-2016). **D.** Bohemanneset (2025). **E.** Svalbard Lufthavn (2015-2025). **F.** Platåberget III (2018-2025). **G.** Longyeardalen – Central (2024-2025). **H.** Adventdalen (2017-2025). **I.** Kapp Thordsen (2025). **J.** Narveneset (2025). **K.** Pyramiden (2015-2023). **L.** Isfjorden – Gåsøyane (2025). **M.** Nedre Sassendalen (2021-2025).

References

NPI Map Data and Services: https://geodata.npolar.no/, last access: 10 April 2025.

ESA, EC: https://apps.sentinel-hub.com/eo-browser/, last access: 26 November 2023.

ChiPlot: https://www.chiplot.online/, last access: 18 August 2023.

Auer, A. G., Van Der Bilt, W. G. M., Schomacker, A., Bakke, J., Støren, E. W. N., Buckby, J. M., Cederstrøm, J. M., and Van Der Plas, S.: Hydroclimate intensification likely aided glacier survival on Svalbard in the Early Holocene, Commun Earth Environ, 6, 100, https://doi.org/10.1038/s43247-025-02064-z, 2025.

Bertrand, S., Tjallingii, R., Kylander, M. E., Wilhelm, B., Roberts, S. J., Arnaud, F., Brown, E., and Bindler, R.: Inorganic geochemistry of lake sediments: A review of analytical techniques and guidelines for data interpretation, Earth-Science Reviews, 249, 104639, https://doi.org/10.1016/j.earscirev.2023.104639, 2024.

Blanchet, C. L., Thouveny, N., and Vidal, L.: Formation and preservation of greigite ($Fe_3 S_4$) in sediments from the Santa Barbara Basin: Implications for paleoenvironmental changes during the past 35 ka, Paleoceanography, 24, 2008PA001719, https://doi.org/10.1029/2008PA001719, 2009.

Boyall, L., Valcárcel, J. I., Harding, P., Hernández, A., and Martin-Puertas, C.: Disentangling the environmental signals recorded in Holocene calcite varves based on modern lake observations and annual sedimentary processes in Diss Mere, England, J Paleolimnol, 70, 39–56, https://doi.org/10.1007/s10933-023-00282-z, 2023.

Davies, S. J., Lamb, H. F., and Roberts, S. J.: Micro-XRF Core Scanning in Palaeolimnology: Recent Developments, in: Micro-XRF Studies of Sediment Cores: Applications of a non-destructive tool for the environmental sciences, edited by: Croudace, I. W. and Rothwell, R. G., Springer Netherlands, Dordrecht, 189–226, https://doi.org/10.1007/978-94-017-9849-5_7, 2015.

196 Dietze, M., Schulte, P., and Dietze, E.: Application of end-member modelling to grain-size
197 data: Constraints and limitations, Sedimentology, 69, 845–863,
198 https://doi.org/10.1111/sed.12929, 2022.

199 Hobday, A. J., Alexander, L. V., Perkins, S. E., Smale, D. A., Straub, S. C., Oliver, E. C. J.,
200 Benthuysen, J. A., Burrows, M. T., Donat, M. G., Feng, M., Holbrook, N. J., Moore, P. J.,
201 Scannell, H. A., Sen Gupta, A., and Wernberg, T.: A hierarchical approach to defining marine
202 heatwaves, Progress in Oceanography, 141, 227–238,
203 https://doi.org/10.1016/j.pocean.2015.12.014, 2016.

204 Küchler-Krischun, J. and Kleiner, J.: Heterogeneously nucleated calcite precipitation in Lake
205 Constance. A short time resolution study, Aquatic Science, 52, 176–197,
206 https://doi.org/10.1007/BF00902379, 1990.

207 Kylander, M. E., Ampel, L., Wohlfarth, B., and Veres, D.: High-resolution X-ray
208 fluorescence core scanning analysis of Les Echets (France) sedimentary sequence: new
209 insights from chemical proxies: XRF CORE SCANNING ANALYSIS OF LES ECHETS
210 SEDIMENTARY SEQUENCE, J. Quaternary Sci., 26, 109–117,
211 https://doi.org/10.1002/jqs.1438, 2011.

212 Lotter, A. F., Sturm, M., Teranes, J. L., and Wehrli, B.: Varve formation since 1885 and high-
213 resolution varve analyses in hypertrophic Baldeggersee (Switzerland), Aquatic Science, 59,
214 304–325, https://doi.org/10.1007/BF02522361, 1997.

215 Mazurek, M., Paluszkiewicz, R., Rachlewicz, G., and Zwoliński, Z.: Variability of Water
216 Chemistry in Tundra Lakes, Petuniabukta Coast, Central Spitsbergen, Svalbard, The
217 Scientific World Journal, 2012, 1–13, https://doi.org/10.1100/2012/596516, 2012.

218 MET Norway: https://seklima.met.no/, last access: 2 January 2026.

Ohlendorf, C. and Sturm, M.: Precipitation and Dissolution of Calcite in a Swiss High Alpine Lake, Arctic, Antarctic, and Alpine Research, 33, 410–417, https://doi.org/10.1080/15230430.2001.12003449, 2001.

Perkins-Kirkpatrick, S. E. and Lewis, S. C.: Increasing trends in regional heatwaves, Nat Commun, 11, 3357, https://doi.org/10.1038/s41467-020-16970-7, 2020.

Porter, C., Howat, I., Noh, M.-J., Husby, E., Khuvis, S., Danish, E., Tomko, K., Gardiner, J., Negrete, A., Yadav, B., Klassen, J., Kelleher, C., Cloutier, M., Bakker, J., Enos, J., Arnold, G., Bauer, G., and Morin, P.: ArcticDEM - Mosaics, Version 4.1 (1.0), https://doi.org/10.7910/DVN/3VDC4W, 2023.

Prins, M. A. and Weltje, G. J.: End-member modeling of siliciclastic grain-size distributions: The late Quaternary record of aeolian and fluvial sediment supply to the Arabian Sea and its paleoclimatic significance, in: Numerical experiments in stratigraphy: Recent advances in stratigraphic and sedimentologic computer simulations, edited by: Harbaugh, J., Society for Sedimentary Geology, 91–111, 1999.

Stachowska, Z., Van Der Bilt, W. G. M., and Strzelecki, M. C.: Coastal lake sediments from Arctic Svalbard suggest colder summers are stormier, Nat Commun, 15, 9688, https://doi.org/10.1038/s41467-024-53875-1, 2024.

Strzelecki, M. C., Lindhorst, S., Hein, C. J., van der Bilt, W. G. M., Kivimaki, K. E., and Kavan, J.: 10,000 years of centennially-resolved climate and sea-level change archived in Svalbard beach-ridge system, Sci Rep, https://doi.org/10.1038/s41598-025-33652-w, 2026.

Toonen, W. H. J., Winkels, T. G., Cohen, K. M., Prins, M. A., and Middelkoop, H.: Lower Rhine historical flood magnitudes of the last 450years reproduced from grain-size

241 measurements of flood deposits using End Member Modelling, CATENA, 130, 69–81,
242 https://doi.org/10.1016/j.catena.2014.12.004, 2015.

243 Vanderploeg, H. A., Eadie, B. J., Liebig, J. R., Tarapchak, S. J., and Glover, R. M.:
244 Contribution of Calcite to the Particle-Size Spectrum of Lake Michigan Seston and Its
245 Interactions with the Plankton, Can. J. Fish. Aquat. Sci., 44, 1898–1914,
246 https://doi.org/10.1139/f87-234, 1987.